UNIVERSIDAD DE CHILE
FACULTAD DE CIENCIAS FÍSICAS Y MATEMÁTICAS
DEPARTAMENTO DE ASTRONOMÍA

THE EVOLUTION OF THE GALAXY STELLAR MASS FUNCTION FROM $Z \sim 2$ TO $Z \sim 5$

TESIS PARA OPTAR AL GRADO DE
MAGÍSTER EN CIENCIAS, MENCIÓN ASTRONOMÍA

DANIELA VICTORIA BARRIENTOS ACEVEDO

PROFESOR GUÍA:
VALENTINO GONZÁLEZ CORVALÁN

MIEMBROS DE LA COMISIÓN:
GUILLERMO BLANC MENDIBERRI
MÉDÉRIC BOQUIEN
WALTER MAX-MOERBECK ASTUDILLO

Este trabajo ha sido parcialmente financiado por Fondecyt Iniciación nro. 11160832

SANTIAGO DE CHILE
2019

RESUMEN DE LA MEMORIA PARA OPTAR
AL TÍTULO DE MAGÍSTER EN CIENCIAS, MENCIÓN ASTRONOMÍA
POR: DANIELA VICTORIA BARRIENTOS ACEVEDO
FECHA: 2019
PROF. GUÍA: VALENTINO GONZÁLEZ CORVALÁN

THE EVOLUTION OF THE GALAXY STELLAR MASS FUNCTION FROM $Z \sim 2$ TO $Z \sim 5$

La Función de Masa Estelar de Galaxias (GSMF) es una herramienta muy importante para estudiar la evolución de galaxias a través del tiempo. Corresponde a una medición de la densidad de número de galaxias por rango de masas. Su forma es afectada directamente por los procesos físicos que regulan la formación estelar en las galaxias, lo que la convierte en un excelente medio para seleccionar modelos de evolución. Sin embargo, la construcción de la GSMF típicamente se lleva a cabo usando métodos de selección diferentes a distintas etapas del universo ($z \leqslant 3$ y $z \geqslant 4$), lo que dificulta el estudio de la evolución de su forma. Por otro lado, obtener estimaciones de masa confiables se hace difícil a alto redshift, donde la señal a ruido en las observaciones del óptico (en sistema de referencia en reposo) es menor y los efectos de la contribución de la emisión nebular no han sido observados directamente.

En este trabajo presentamos nuevas estimaciones de la Función de Masa Estelar de Galaxias desde $z \sim 2$ a $z \sim 5$ realizando una selección homogénea de fuentes en todo este rango mediante criterios de color-color. Utilizando fotometría de gran profundidad de HST y aprovechando las observaciones más profundas realizadas con el telescopio espacial Spitzer del programa GREATS (PI: Labbé; Stefanon et al. 2019, in prep.), determinamos la masa estelar para una muestra de $\sim$ 16000 galaxias, extendiendo nuestro límite de detección a $M_* \sim 10^7 M_\odot$. Nuestras GSMF fueron creadas transformando las Funciones de Luminosidad en el UV de Bouwens et al. (2019, in prep) y usando relaciones $\log_{10}(M_*)$–$M_{\rm UV}$ obtenidas de nuestras observaciones a cada redshift. Observamos que existe una relación notoria entre la masa estelar y la magnitud absoluta en el UV para todos los redshifts de este estudio. Nuestros modelos lineales muestran una evolución en la normalización de estas relaciones, mientras que la pendiente en ellas parece mantenerse. De nuestro estudio de la dispersión intrínseca de esta relación encontramos que esta se mantiene constante para nuestras muestras a $z \sim 2,\ 3$ y 4 pero luego decrece a $z = 5$.

Luego de parametrizar nuestras GSMF usando funciones de Schechter estudiamos la evolución de sus parámetros poniendo énfasis en la evolución de α, la pendiente del extremo de baja masa. Encontramos una evolución tanto en la normalización de nuestras GSMFs, Φ^*, como en la pendiente, α, disminuyendo con el redshift. La masa característica de nuestros modelos, por el contrario, no presenta una clara evolución. También calculamos la densidad de masa estelar resultante de nuestras GSMF y encontramos un aumento de esta desde $z \sim 5$ a $z \sim 2$. Al comparar nuestros resultados con las predicciones provenientes de la evolución de la densidad de la tasa de formación estelar (SFRD), nuestras estimaciones son consistentes con las predicciones de Madau and Dickinson (2014) a $z \sim 4$ y 5, pero discrepan a $z \sim 2$ y 3, siendo más bajas que lo predicho.

A mi familia.

Agradecimientos

Quiero agradecer encarecidamente el apoyo incondicional que he recibido de mi familia durante esta y todas las etapas de mi formación como profesional. Si he logrado cumplir mis objetivos, es porque ellos siempre estuvieron ahí para apoyarme.

Agradezco también, a todos los profesores que han ayudado en mi formación como investigadora y especialmente a Valentino González, quien ha sido mi guía durante este intenso periodo. Le agradezco por creer en mis capacidades y por ayudarme a crecer como científica.

Además, me gustaría agradecer a todos los amigos que me acompañaron durante este proceso. Aunque no nos viésemos muy seguido nuestros ratos de encuentro siempre me dieron un agradable respiro en esta estresante etapa.

Por último, quiero agradecer la compañía de todos los compañeros que conocí durante estos años, especialmente aquellos con los que compartí oficina (los cala(n)bozos). Nuestros almuerzos y momentos de esparcimiento juntos hicieron de Calán un lugar menos hostil. Siempre los voy a recordar con mucho cariño.

Contents

Introduction **1**
0.1 Estimating the Stellar Mass of high redshift galaxies . . . 1
0.2 The Galaxy Stellar Mass Function . . . 3
0.3 This work . . . 5

1 Data **7**
1.1 Data Sets . . . 7
1.1.1 3DHST . . . 8
1.1.2 HST/ACS and WFC3/IR Photometry . . . 8
1.1.3 Spitzer/IRAC and K_S–band Photometry . . . 8
1.2 Sample Selection . . . 9

2 SED Modeling **12**
2.1 Fitting Procedure . . . 12
2.1.1 Maximum Likelihood vs Bayesian Stellar Masses . . . 14
2.1.2 The Main Sequence of Star Forming Galaxies and its outliers . . . 16
2.2 Effects of Nebular Emission . . . 21

3 The Stellar Mass Functions **28**
3.1 Rest Frame UV Luminosity . . . 28
3.2 The $\log_{10}(M_*)$ vs. $M_{\rm UV}$ Relation . . . 29
3.3 Galaxy Stellar Mass Functions . . . 37
3.3.1 Computation of the Mass Function . . . 37
3.3.2 Schechter Fit . . . 38
3.4 Stellar Mass Densities . . . 43

Conclusion **47**

Bibliography **50**

List of Tables

2.1 Parameters and their values used to generate our SED models. 13
2.2 Summary of the emission lines considered for our study of the effects of Nebular Emission on our mass estimates. Indicated are the redshift ranges in which these lines enter the transmission curves of the photometric bands affected at ~ 4, and 5. 23

3.1 Photometric bands used to compute $M_{\rm UV}$ for all our selected redshift samples. 29
3.2 Best fit parameters for $\log_{10}(M_*)$-$M_{\rm UV}$ 34
3.3 Galaxy Stellar Mass Functions for all redshifts considered in this study. Lower and upper uncertainties were computed as the 16th and 84th percentiles from the distribution of number density per mass bin. 38
3.4 Best-fit Schechter parameters and their 1σ uncertainties for our GSMFs at $z = 2$–5. 41

List of Figures

1.1 Distributions of redshift obtained through SED modeling for each of the selected bins. For the two highest redshift bins $z \sim 4, 5$ bands with potential contribution from nebular emission lines were excluded from this computation, leaving the constraining of the redshift mostly to the rest-frame UV continuum shape. 11

2.1 Example probability distribution functions for some of the parameters estimated using our chosen SED fitting technique on sources with high stellar mass offsets between the MLE and Bayesian estimates, as indicated in Figure 2.3. From left to right the marginalized posterior distributions for stellar mass, age and extinction in the V band, A_V, are shown. The top row corresponds to a galaxy with multimodal posteriors, where the probability density function (PDF) of stellar mass and age present more than one local maxima. On the lower row the distributions are asymmetrical, which also leads to inconsistencies in the estimated values. 15

2.2 Similar to Figure 2.1, the PDFs of stellar mass, age and V-band extinction are shown. Both the source at the top and bottom row have low offsets < 0.3 dex in estimated mass and in this case the marginalized distributions appear more symetric than those shown in Figure 2.1. 16

2.3 Distribution of offsets between Bayesian and MLE estimations of stellar mass for all redshifts studied in this thesis. Vertical dashed blue lines indicate the median of the distributions shown, for all redshifts considered, this value is close to zero. Vertical dashed red lines encase sources with differences lower than a factor $\times 2$. The fraction of the distribution contained inside these lines correspond to $\sim$ 89%, 92%, 93% and 90% at redshifts $z \sim 2,\ 3,\ 4$, and 5, respectively. 17

2.4 Distributions of offsets between Bayesian and MLE estimations of SFR for all redhsifts considered in the study. Dashed blue lines indicate the medians of the distributions with values consistently > 0 at all redshifts. Dashed red lines indicate the -1 and 1 dex limits, representing differences of a factor $\times 10$ in the estimated values. Around a 60% of the samples at each redshift lie inside these limits. All distributions present long tails reaching values of $\log_{10}(SFR_{\rm bayes}/SFR_{\rm best}) \sim 15$ where the MLE model solution is that of a quiescent galaxy. 18

2.5 Stellar mass M_* vs SFR distributions at redshift $z \sim 4$. The values used in the left panel correspond to the Bayesian estimates while the right panel shows the distributions obtained from the MLEs. In blue, the main sequence relation computed by Whitaker et al. (2014) for sources at $2.0 < z < 2.5$, their highest redshift bin. The increase in SFR at a given M_* shown in panel a) compared to Whitaker et al. (2014) relation is consistent with the redshift evolution of this relationship. Grey dashed lines indicate tracks of constant sSFR. 20

2.6 Kernel density estimate of the distributions of specific star formation rates for our galaxy populations at each redshift bin. Only star-forming galaxies are considered in this figure, excluding galaxies with $\log_{10}(sSFR) \leq -10$. The vertical black line at -7.6 separates the main sequence sources from the cloud of high SFR as indicated by Caputi et al. (2017). 21

2.7 2D distributions of age and dust extinction for the population at $z \sim 4$. Each point represents a galaxy in our catalog, and the contours represent the 2D density levels. On the left panel the estimations used correspond to the Bayesian procedure, while the right panel shows our MLE values for each galaxy. The MLE were perturbed using a normal distribution of size 0.1 for presentation purposes. 22

2.8 Example model SEDs showcasing some of the effects rest-frame optical emission lines have on the integrated fluxes for galaxies at $z \sim 4$, 5. 24

2.9 Distribution of mass offsets for our sample at $z \sim 4$ from varying the amount of photometric bands included in the SED fitting, as a test of the contribution from nebular emission. The offsets correspond to the difference in estimated Bayesian masses when excluding potentially contaminated bands by emission lines, and using all the available bands. In red the distribution shows the offset in mass caused by the flux contribution from Hα. The distribution in blue is the control group of galaxies with $z < 3.8$, where the flux in [3.6] is not enhanced by any lines. Vertical dashed lines indicate the mean of the distributions, where the control group has an offset of -0.02 dex and the contaminated galaxies, at $z > 3.8$ have a bigger offset of -0.07. 25

2.10 Mass offsets for galaxies in the $z \sim 5$ bin. In this case the only band removed from the SED fitting is [3.6]. We separate our sample between galaxies at $z < 5.0$ (in blue), where the contribution of nebular emission lines is restricted to the [3.6] channel. At $z > 5.4$ (in red), Hα has moved to [4.5] and [3.6] has flux contributions from both the [O III] and Hβ lines. The lower redshift sample shows the offsets generated by $H\alpha$, similar to what is shown in Figure 2.9 for the sample at $z > 3.8$. On the other hand, the sample at $z > 5.4$ shows the effect of adding the other two lines to the fitting. Vertical dashed lines of the same colors show the mean of each distribution with values of -0.08 dex and 0.03 dex respectively. 26

3.1 Stellar log mass (M_*) vs. rest-frame UV absolute magnitude at 1600Å ($M_{\rm UV}$) distributions for $z = 2$–5. Small blue circles represent individual galaxies in our samples with S/N $\geqslant 3$ in [3.6] and white squares represent galaxies with S/N < 3. Error bars correspond to the 1σ uncertainties in both estimations of mass and absolute magnitude. Red squares correspond to the median masses in absolute magnitude bins of size 0.5 mag and their respective errorbars represent the standard deviation of the group. In yellow circles the masses derived from stacked photometry in the same magnitude bins is shown. Our best-fit model trends are traced by a solid red line at each redshift, and the shaded red area corresponds to the width of the intrinsic scatter found by our MCMC exploration of parameter space. Also plotted are the best-fit trends from Song et al. (2016) (in dashed green lines) and Duncan et al. (2014) (in cyan dashed lines) at $z \sim 4$ and 5. 32

3.2 Median flux stacked SEDs at $z = 2$–5. Stacks were performed in bins of rest-frame UV magnitude with $\Delta M_{\rm UV} = 0.5$ mag with more than 5 galaxies. The stacked fluxes are represented by filled circles and errorbars corresponding to their 1σ uncertainty. Downward pointing arrows indicate sources with S/N < 2. Unfilled squares correspond to those bands not used in the SED fitting, we leave out all bands bluewards of the Lyman limit, and H_{160} at $z \sim 4$ since in the $3.5 < z < 4.5$ range it is positioned at the Balmer Break ($\lambda_{\rm rest} = 3646$ Å) . The solid lines indicate our best-fit models. Stacked fluxes and models are color-coded by their UV absolute magnitude bins, as indicated in the legend. 33

3.3 All best-fit trends obtained from our model fitting procedure at $z = 2$–5. . . 34

3.4 Comparison of best-fit trends for $\log_{10} M_*$ and $M_{\rm UV}$ when controlling for nebular emission and not. Dashed lines correspond to the trends obtained from using masses derived from all the available photometry, while solid lines were derived from our estimations of mass corrected by the effects of nebular emission lines. We also show the different trends obtained from using the contaminated sample (in red and black) and the control group (in blue and cyan). . 36

3.5 Evolution of the UV-LFs used in this study and the resulting GSMFs obtained from them. Solid lines indicate the Schechter fits for both luminosities and stellar masses. Filled circles represent our estimated GSMF and their corresponding 1σ errors. 39

3.6 Our galaxy stellar mass functions from LBG selected sources at $z = 2$–5 in red filled circles and their respective 1σ errors. The solid red lines represent our best-fit Schechter functions and the light-pink lines correspond to 500 draws from the joint posterior distributions obtained through our MCMC fit. Previously computed GSMF at redshift ranges similar to ours from the literature are plotted beside our mass functions. Mortlock et al. (2015) (Mo+15 in the legend), Davidzon et al. (2017)(Da+17), Duncan et al. (2014)(Du+14), Grazian et al. (2015)(Gr+15), Song et al. (2016)(So+16) and González et al. (2011)(Go+11). Conversion to a Chabrier IMF were applied when needed. 40

3.7 Confidence contours of the best-fit Schechter parameters for our GSMFs at $z = 2$–5 at the 68% and 95% levels. 42

3.8 Redshift evolution of the best-fit Schechter parameters for our GSMFs. Lower and upper uncertainties correspond to the 16th and 84th percentiles from the posterior distributions obtained from our MCMC fitting. A linear trend is fitted for the evolutions of Φ^* and α with redshift in blue. 44
3.9 Evolution of the Schechter parameter α, the low-mass end slope for our GSMFs (yellow circles). Beside them, previous estimates from the literature are shown. 45
3.10 Evolution of the stellar mass density with redshift. Our stellar mass density estimations were computed by integrating the best-fit Schechter functions for our GSMFs between $M_* = 10^8 M_\odot$ and $M_* = 10^{13} M_\odot$. Yellow filled circles correspond to our estimations using single Schechter functions while in blue are the result from using a double Schechter function at the lower redshift ranges. Uncertainties were obtained by performing 10^4 repetitions perturbing our GSMFs using the posterior distributions for the Schechter parameters. Overplotted are some results from the literature. A dashed black curve indicates the predicted SMD from Madau and Dickinson (2014) SFRD using a recycling factor of $R = 0.41$. 48

Introduction

The ability to image the high redshift universe through deep surveys that go from the UV all the way to the near-infrared in their wavelength coverage has extended our knowledge of the first stages of galaxy evolution in the past decades. Not only it has become possible to photometrically select (Ellis et al., 2013; Oesch et al., 2013) and detect galaxies as far back as $z \sim 9$–10 (~ 500 Myrs after the Big-Bang; Zitrin et al., 2015; Oesch et al., 2016), but also the wealth of multiwavelength data for sources at lower redshifts ($1 < z < 6$) has enabled statistical studies of their physical properties (Barro et al., 2019; Labbé et al., 2010a), helping to shed light onto the mechanisms that drive galaxy formation and evolution.

Studies exploring galaxy evolution throughout cosmic time often look at the distributions of quantities like the star formation rate (SFR) and stellar mass (M_*) of a population. Both of these are measurements of the growth of galaxies, one instantaneous, SFR; the other cumulative, M_*; and following their evolution with redshift provides a picture of the rate at which galaxies have assembled mass. Estimating stellar mass and SFR for galaxies at all redshifts has become a fundamental task to inform models of galaxy evolution.

Of special interest is the redshift range between $2 < z < 4$, where the peak of SFR density (SFRD) occurs Madau and Dickinson (2014). This epoch is when galaxies are growing the fastest, so having studies of how stellar mass is evolving during this time is crucial.

0.1 Estimating the Stellar Mass of high redshift galaxies

A widely used approach to estimate quantities like SFR and stellar mass is through stellar population modeling. The physical properties of unresolved stellar populations can be inferred from their spectral energy distributions (SED) by trying to reproduce its shape using synthetic spectra.

The first step in the creation of a model for the stellar contribution in a galaxy is to represent the spectrum of a simple stellar population (SSP), a population of stars born in the same burst of star formation at a single metallicity. This requires an initial mass function (IMF), to define the number distribution of masses of the stars created in the burst. Isochrone tracks then determine the relation between $T_{\rm eff}$, $\log g$ and M_* and each star gets assigned a stellar type. Stellar population synthesis (SPS) codes take this information and use individual stellar spectra from libraries to create a spectrum corresponding to the whole population of

these stars.

Adding information on the chemical evolution of these stars and a star formation history (SFH), to dictate the rates at which new populations arise, these codes produce spectra for composite stellar populations (CSP). The emission and absorption produced by the gas and dust in the ISM can also be added to the final spectra, representing all the components in a galaxy (see Conroy, 2013 for a more thorough description).

When we convolve these spectra with a set of transmission curves we obtain fluxes that we can compare to observations from our galaxies and learn about their physical properties like metallicties, ages, and M/L ratios. Stellar masses, in particular come from the scaling of these models to the observed fluxes in a galaxy. The best-fit mass will be given by the set of parameters that can best reproduce the colors and brightness of our galaxies.

At high redshift, the Hubble Space Telescope's (HST) *Advanced Camera for Surveys* (ACS) and *Wide Field Camera 3* (WFC3) provide deep broad-band multi-wavelength photometry of the rest-frame UV, going from the Lyman break at 912 Å to the 4000 Å break for galaxies at $z \sim 4$. The emission at this wavelength range is mostly produced by massive O and B stars with short main sequence lives of $\sim$ 10–100 Myrs, making it a good tracer for recent star formation. However, determining masses using only the UV continuum leads to very large uncertainties due to the short time scales in which this radiation varies. Lower mass stars, which take longer to evolve, emit most of their light at longer wavelengths. They are also more abundant so they contribute a large portion of a galaxy's mass. But their UV fluxes get "outshined" in the UV by the very young and bright stars, and their contributions can get lost (Papovich et al., 2001). So, observations of the rest-frame optical and near-infrared ($\lambda_{\rm rest} > 4000$ Å) that can explore this older and longer lived stellar population, become essential to constrain the stellar masses of high-z sources.

With today's technology reliable estimates of stellar mass for galaxies at $z \gtrsim 4$ can only be achieved using Spitzer's *Infra-Red Array Camera* (IRAC) to image galaxies in their rest-frame optical. These kinds of measurements have only been possible since sufficiently deep Spitzer data became available to make detections of HST-identified sources on these images. Achieving this depth takes long integration times, becoming a difficult task. On top of that, the point spread function (PSF) of Spitzer is larger than HST's, with a full width at half maximum (FWHM) $\sim 1\farcs7$ at 3.6 μm against $\sim 0\farcs19$ at 1.6 μm with WFC3. So, crowding becomes an issue when doing long integrations with IRAC and special procedures need to be applied to extract photometry from these images.

In addition to the uncertainties brought by the lack of deep MIR data, it has been pointed out by some studies (Schaerer and De Barros, 2009) that the addition of Nebular Emission to the SED models can cause significant differences on the physical properties derived through SED modeling at $z \gtrsim 4$. Young high mass stars ionize the gas surrounding star forming regions, and we would expect to see nebular emission lines in the range of our observations. This added flux to our photometry changes the shape of the observed broad-band SEDs and if not taken into account correctly, changes the derived physical parameters. This effect becomes more prominent at high redshift because due to the redshifting of the spectrum features of a given equivalent width will occupy a larger fraction of a band compared to rest frame.

Recent studies of the physical properties of galaxies at high redshift have started to add nebular emission to their models to account for this effect (e.g. Salmon et al. 2015; Song et al. 2016). However, incorporating this contribution into our synthetic spectra is not an easy task. To obtain reliable models we need information on the intensity of these lines and how they relate to the physical conditions of the gas where they form. But at $z \gtrsim 3$ this emission gets redshifted to the MIR and obtaining spectroscopic observations of them is impossible with today's instrumentation.

Some studies have tried to estimate this contribution, and the effects they produce in our estimates of the physical parameters, by studying IRAC colors of galaxies at these redshifts. Stark et al. (2013), find reduction factors of about $\times 1.2$ for stellar masses at $z \sim 4$ and 5 when studying the excess flux produced by the Hα line in the [3.6] IRAC channel. To get a direct solution to this issue we will have to wait until the launch of the James Webb Space Telescope (JWST) in the near future, which will bring the ability to take direct spectra of Hα emission in galaxies up to $z \sim 6$.

0.2 The Galaxy Stellar Mass Function

The stellar mass provides a measurement of the cumulative growth in a galaxy, containing information about the processes that are involved in mass assembly, including star formation, galaxy mergers, supernova feedback, AGN feedback, etc. The Galaxy Stellar Mass Function (GSMF), a measurement of the number density of galaxies per mass bin, is modeled by these processes, making it an important tool to test evolutionary models that account for these effects.

The shape of the GSMF is generally well described by a Schechter function (Schechter, 1976). This function consist of a power law at the low-mass end followed by an exponential fall at masses larger than some characteristic mass. This function is parameterized by a normalization, Φ^*; a characteristic mass, M^*, at which the function changes shape; and the slope of the low-mass end, α.

Discrepancies between the observed shape of the GSMFs and results from simulations are found in both semi-analytic models (SAMs) and cosmological hydrodynamical simulations at redshifts $z > 0.5$ (Marchesini et al., 2009; Weinmann et al., 2012; Vogelsberger et al., 2013). Simulations that don't take into account star-formation feedback end up with a higher amount of low mass galaxies than those observed (Fontanot et al., 2009), thus affecting the values of the low-mass end slopes of the predicted GSMFs. Slowing down star formation can be done trough various mechanisms, some processes inject energy into the gas preventing it from cooling enough to form stars while others remove the gas around star forming regions (see Somerville and Davé 2015). All of these processes have a different impact on the amount of low mass sources generated, resulting in different values for the low-mass end slope (Vogelsberger et al., 2013).

Having better constraints on the low-mass end slope could also help to clear up the inconsistencies between the estimations of Stellar Mass Density (SMD), coming from integrating

GSMFs, and those inferred from integrating the Star Formation Rate Density (SFRD) over time. Both these quantities measure the evolution of galaxy growth through mostly independent measurements, so it is important that they provide consistent result to get a correct picture of galaxy evolution. Madau and Dickinson (2014) reports a ~ 0.2 dex difference between their predicted SMDs and those observed by multiple works at $0 < z < 3$ (Madau and Dickinson (2014), and references therein). It has been proposed by Santini et al. (2012), that a steepening of the low-mass end slope would alleviate some of the discrepancies at the $2 < z < 4$ range, around the peak of SFRD.

Even so, recent studies have reported conflicting results regarding both the value of the low-mass end slope and its evolution with redshift. Evidence both supporting and disregarding a steepening of the slopes with redshift can be found in the literature from studies of low and high redshift samples (Marchesini et al., 2009; Santini et al., 2012; Ilbert et al., 2013; Duncan et al., 2014; Grazian et al., 2015; Song et al., 2016; Davidzon et al., 2017).

Duncan et al. (2014) and Grazian et al. (2015) constructed GSMFs at $4 < z < 7$ using data from the Cosmic Assembly Near-infrared Deep Extragalactic Legacy Survey (CANDELS; Grogin et al., 2011; Koekemoer et al., 2011), the former presented steeper than previously found low-mass end slopes of ~ -1.89 with no indication for evolution, while the latter found slightly shallower slopes of -1.63 – -1.88 and no strong evolution either. At lower redshifts, Marchesini et al. (2009) also reports no evidence for an evolution of the slopes for galaxies at $1.3 < z < 4.0$, when uncertainties due to SED-modeling assumptions are taken into account.

On the other hand, Santini et al. (2012) published a steepening of the low-mass end slope going from -1.44 at $z \sim 0.8$ to -1.86 at $z \sim 3$, but they reported that this evolution stalled at higher redshifts. Most recently, evidence supporting the steepening of the slopes with redshift was presented by Song et al. (2016). In their study of ~ 4500 galaxies in the CANDELS/GOODS and HUDF fields they computed GSMFs at $z = 4$–8, and their estimations of the low-mass end slope evolved from -1.55 to -2.25 increasing with redshift.

While there are clear discrepancies in the results presented at the same redshift bins, there is also a disconnect between redshift regimes. An issue that arises in the computation of the GSMF is the effect of sample incompleteness and selection biases that exist in studies of stellar mass. Furthermore, at different redshift regimes the approaches used to deal with this problem vary. At lower redshifts $1 < z < 4$, techniques like the $1/V_{max}$ estimator(Schmidt, 1968) and maximum likelihood methods (Efstathiou et al., 1988; Sandage et al., 1979), that aim at estimating the incompleteness of a sample and correcting for it to build GSMFs are widely used. However these methods become harder to apply as we go to higher redshift.

Studies at $z > 4$ have avoided this problem by using UV luminosity functions (UV-LFs) to derive their stellar mass counterparts by transforming luminosity samples into stellar masses through a M_*–$L_{\rm UV}$ relation (e.g. González et al. 2011; Grazian et al. 2015; Song et al. 2016). This method takes advantage of the fact that selection effects are much better understood and easier to estimate for the derivation of the UV-LF.

The differences in methodologies make it difficult to follow the evolution of the GSMF parameters and assessing the discrepancies in their results through the crucial $z \sim 3$ epoch,

the peak of the global star formation. Davidzon et al. (2017) make an effort to estimate the evolution of mass assembly using a consistent method from local $z = 0.1$ to high $z = 6$ galaxies. They compute GSMF for galaxies in the COSMOS field using completeness correction techniques that yield results supporting an evolution of the low-mass end slope, decreasing from -1.47 at $z = 0.1$ to -2.11 at $z = 5$. However their $1/V_{\rm max}$ estimations of the GSMF only reach masses around $\sim 10^{9.5} M_\odot$ – $10^{10} M_\odot$ at their highest redshift bins, which are not low enough to place strong constraints on the low-mass end slope.

0.3 This work

The aim of this thesis is to provide consistent determinations of the galaxy stellar mass function from $z \sim 2$ to $z \sim 5$, with special emphasis on the study of the robustness of our stellar mass estimates. We use an homogeneous method to select samples at all redshifts probed in this study by using all of the deep observations available from HST archival data in the CANDELS fields. Our GSMFs are constructed by combining rest-frame UV luminosity functions derived from this data (Bouwens et al. 2019, in prep., internal communication) and our determinations of the relationship between stellar mass and rest-frame UV absolute magnitude at each redshift.

Using the deepest Spitzer/IRAC observations to date from the GREATS survey (PI: Labbé; Stefanon et al. 2019, in prep., internal communication) we expect to extend the mass completeness limits on our GSMFs and provide good constraints on the computation of the low-mass end slopes and its evolution. We propose an alternative method to control for the effects the intensity of rest-frame optical lines produce in our estimations of stellar mass that doesn't involve choosing nebular emission prescriptions. We also explore the effects of using different M_* estimates (e.g., maximum likelihood vs. Bayesian marginalized posterior estimates) in our determinations of the GSMFs and their parameters. We use our determinations of the GSMF to derive SMDs for our samples and compare them to previous results from the literature.

This thesis is organized as follows. Chapter 1 describes the data used to estimate stellar masses and UV luminosities and the selection criteria used to separate our sources in redshift bins. Then, an explanation of the procedures used to model the stellar mass for each galaxy and the robustness of our estimates are discussed in Chapter 2. We dedicate Section 2.2 of this chapter to discuss the method we used to control for the effects of nebular emission. Finally Chapter 3 deals with the construction of our GSMFs and the results obtained at $z = 2,\ 3,\ 4,$ and 5. We divide this chapter in three main parts, in Section 3.2 we start by presenting our $\log_{10}(M_*)$ vs. $M_{\rm UV}$ distributions and the best-fit trend obtained at each redshift. From the combination of these relations and Luminosity Functions from the literature we construct the Mass Functions shown in Section 3.3. We also provide a detailed explanation of the procedure and our estimations of the best-fit Schechter parameters and their evolution. We finish with our estimations of the SMD and its evolution followed by a discussion of our results and how they compare with the literature in Section 3.4.

All magnitudes listed in this thesis use the AB magnitude system. We use a ΛCDM

cosmology with $\Omega_M = 0.27$, $\Omega_\Lambda = 0.73$ and $H_0 = 70.4$ km s^{-1}Mpc^{-1}, where needed.

Chapter 1

Data

1.1 Data Sets

The stellar masses presented in this work were computed using deep multiwavelength data for a large sample of star-forming galaxies in the range $2 < z < 5$. Our samples at $z \sim 2$ and 3 were taken from a previous selection of sources over the CANDELS GOODS-South and GOODS-North fields (Giavalisco et al., 2004) performed by Bouwens et al. (2019, in prep, internal communication).

Using photometry from the HDUV (Oesch et al., 2018) and UVUDF Teplitz et al. (2013) programs, Bouwens et al. (2019, in prep.) selects 11000 sources at $z \sim 2$–3 in a total area of ~ 100 arcmin^2. The selection is based on the LBG criteria using the WFC3/UVIS UV_{275} and U_{336} filters (further details in Section1.2). Photometry in the rest-frame UV and optical for these sources was obtained by matching our samples with the public 3DHST/CANDELS catalogs (Skelton et al., 2014), from where we get HST and Spitzer coverage for all of our sources.

At $z \sim 4$ and 5 we use the samples selected by Bouwens et al. (2015), based on data from the deepest extragalactic surveys. These include HST observations in the Extreme Deep Field (XDF, Illingworth et al., 2013), the parallel fields HUDF09-1 and HUDF09-2 (Bouwens et al., 2011), and all CANDELS fields (Grogin et al., 2011). The total search area corresponds to ~ 300 arcmin^2 where Bouwens et al. (2015) identifies 8861 sources in the range $4 < z < 5$ using the LBG criteria (see Section 1.2 for details). In addition to the HST/ACS and WFC3/IR data to select the sources we use deep Spitzer/IRAC observations from the GREATS program (PI:Labbé; Stefanon et al. 2019, in prep., internal communication) to estimate the physical parameters — in particular the stellar mass — of the galaxies in this sample.

This sample has already been presented in previous works such as Bouwens et al. (2015), but we provide a short description of the data sets we use and the sample selection in this section. For a more thorough description of both the observations and data reduction refer to (Bouwens et al., 2015, Bouwens et al. 2019, in prep.).

1.1.1 3DHST

To obtain stellar mass estimates for our sources at $z \sim 2$ and 3 we used photometry from the 3D-HST v4.1.5 release (Skelton et al., 2014) in the GOODS-South and GOODS-North fields. Observations in the 3DHST catalogs cover an area of $\sim$ 170 arcmin^2 and 160 arcmin^2 for the GOODS-South and GOODS-North fields, respectively, covering the search area used by Bouwens et al. (2019, in prep.). The catalogs include HST photometry in the B_{435}, V_{606}, i_{775}, z_{850}, J_{125}, JH_{140} and H_{160} bands with a 5σ depth ranging from 25.6 to 27.4 mag depending on the position in the field. Spitzer/IRAC observations in the 3.6μm, 4.5μm, 5.8μm and 8.0μm channels with median 5σ depths of 24.5 mag in the first two channels in GOODS-North field and 24.8 mag in the GOODS-South field were also included in our SEDs. The methods used to construct the catalogs are discussed in detail in (Skelton et al., 2014).

1.1.2 HST/ACS and WFC3/IR Photometry

The photometry at $z \sim 4$ and 5 was taken from the catalogs used in Bouwens et al. (2015), who compiled all archival observations for the CANDELS fields in the B_{435}, V_{606}, i_{775}, I_{814}, z_{850}, J_{125}, JH_{140} and H_{160} HST bands. All the images used were re-reduced using the ACS GTO pipeline APSIS (Blakeslee et al., 2002) and the WFC3/IR pipeline WFC3RED.PY (Magee et al., 2011). The reductions and posterior analysis of the images were performed at a 0.″03–pixel scale for all fields except the CANDELS UDS/COSMOS/EGS ones, where pixel scale is 0.″06. Extraction of the photometry for the HST sources was performed using the SExtractor software (Bertinl, 1996) in dual-image mode. Measurements were made by matching the point-spread function (PSF) of all images to the H_{160} band PSFs and using apertures derived with a Kron (1980) parameter of 1.6.

The deepest observations, reaching $\sim$ 30 mag at 5σ, come from the XDF field covering an area of 4.7 arcmin^2. Observations $\sim$ 1.5–2.5 mag shallower than these are taken over the GOODS-South and GOODS-North fields but covering $\sim$ 30 times more area. CANDELS fields UDS, COSMOS and EGS lack coverage in the B_{435}, i_{775} and z_{850} bands, but are the only ones with K_S imaging and have the widest search area covering $\sim$ 450 arcmin^2 in total.

1.1.3 Spitzer/IRAC and K_S–band Photometry

As described in Section 0.1, rest-frame optical constraints are crucial to derive reliable stellar masses. The photometry in the mid-infrared provided by ground-based CFHT/WIRCam's K_s band and Spitzer/IRAC [3.6] and [4.5] channels is of utmost importance for our SED fitting procedure.

All search fields in Bouwens et al. (2015) catalogs have deep Spitzer/IRAC data from the GOODS (Dickinson et al., 2004), SEDS (Ashby et al., 2013), IUDF (Labbé et al., 2013), and S-CANDELS (Ashby et al., 2015) programs. For the GOODS-South and GOODS-North field we use a combination of all available archival data over [3.6] and [4.5] with observations from the GREATS program obtaining the deepest Spitzer/IRAC detections to date. These

observations and their reduction strategy are presented in Stefanon et al. (2019, in prep).

Due to the broader PSF of Spitzer ($\sim 1\farcs7$ at $3.6\mu m$ compared to HST's $\sim 0\farcs19$ at H_{160}), the effects of source confusion are considerable, and obtaining accurate photometry for these sources becomes more challenging. To obtain the fluxes in these cases the MOPHONGO software (Labbé et al., 2006, 2010a,b, 2013) was used. This code removes the flux from contaminating nearby sources by using the positions and flux profiles from detections in the HST photometry.

The light profiles from all sources in the deep H_{160} images are isolated with independent masks and then convolved with an appropriate kernel to match the larger PSFs in the K_S and IRAC images. The total flux in each of these "templates" is adjusted to fit the fluxes in the K_S–band and IRAC images. The resulting synthetic image is used to subtract the flux from the neighboring sources to our source of interest, isolating it. In the isolation image we perform standard aperture photometry using apertures of $1\farcs2$ for the K_S image, $1\farcs8$ for the [3.6] and [4.5] images and a $2\farcs4$ diameter in the [5.8] and [8.0] images. The measured fluxes are corrected to total, accounting for the flux in the wings of the original PSF, by convolving the HST template to match the broader CFHT and Spitzer PSFs.

We inspect all the residual images to asses the quality of the extraction of neighboring sources. At $z \sim 4$ and 5 we find that $\sim 30\%$ of the sources have residual images where the flux from neighboring sources wasn't completely removed by this process. These sources were removed from our analysis.

1.2 Sample Selection

The separation of the detected sources into redshift bins was performed using Lyman-break-like criteria for the different sets. Broadband photometry in the rest-frame UV can be used to identify star forming galaxies at high redshift by detecting the position of the Lyman break. Most of the radiation produced at $\lambda < 912$Å, the Lyman limit, gets absorbed by the neutral gas surrounding star forming regions. Star forming galaxies have bright UV fluxes, but at wavelengths shorter than this limit the flux will decrease violently generating a drop in the detected flux, this is what is known as the Lyman break. The wavelength of this break will move with redshift, so identifying the wavelength of this drop can give us an estimation of the redshift of the source.

We can detect the position of this break by looking for very red colors in adjacent bands. Then, to distinguish the candidates from intrinsically red sources, bands redward of the break are used to establish the intrinsic color of the source. A final constraint is added to the criteria to make sure there is no flux blueward of the break.

In this work we use the selection of sources performed by Bouwens et al. 2019 (in prep., internal communication) for our samples at $z \sim 2$ and 3, where they use the photometry of the UV_{275} and U_{336} WFC3/UVIS bands from the HDUV and UVUDF programs to establish the position of the break. The criteria used to select sources at $z \sim 2$ and $z \sim 3$ is the

following:

$$(UV_{275} - B_{435} > 1) \wedge ((V_{606} - z_{850} < 0.5) \vee ((UV_{275} - B_{435} > 2(V_{606} - z_{850})) \wedge (V_{606} - z_{850} < 1.0)))$$

or

$$(U_{336} - V_{606} > 1) \wedge ((V_{606} - z_{850} < 0.5) \vee ((U_{336} - V_{606} > 2(V_{606} - z_{850})) \wedge (V_{606} - z_{850} < 1.0))) \wedge (SN(UV_{275}) < 2)$$

Photometric redshifts for the galaxies selected with either of these criteria were obtained using photometric redshift software EAZY Brammer et al. (2008), and sources with best-fit photometric redshifts in the ranges $1.5 < z < 2.5$ and $2.5 < z < 3.5$ were selected in the $z \sim 2$ and $z \sim 3$ samples, respectively.

The selections at $z \sim 4$ and 5 were taken from Bouwens et al. (2015), where they used the following criteria to select sources at $z \sim 4$:

$$(B_{435} - V_{606} > 1) \wedge (\mathrm{i}_{775} - J_{125} < 1) \wedge (B_{435} - V_{606} > 1.6\,(\mathrm{i}_{775} - J_{125}) + 1) \wedge (\text{not in } z \sim 5 \text{ selection})$$

Since the bands available differ from field to field, sources at $z \sim 4$ can not be detected in the UDS, COSMOS and EGS fields, where the lack of B_{435}, i_{775} and z_{850} coverage impedes the search for galaxies with a break in the B_{435} band.

To be selected in the $z \sim 5$ bin, sources had to fulfill the conditions:

$$(V_{606} - \mathrm{i}_{775} > 1.2) \wedge (z_{850} - H_{160} < 1.3) \wedge (V_{606} - \mathrm{i}_{775} > 0.8\,(z_{850} - H_{160}) + 1.2) \wedge (S/N(B_{435}) < 2) \wedge (\text{not in } z \sim 6 \text{ selection})$$

A separate criteria is used to detect sources from the UDS, COSMOS and EGS fields, where the use of i_{775} and z_{850} is replaced by the I_{814} broader filter.

$$(V_{606} - I_{814} > 1.3) \wedge (I_{814} - H_{160} < 1.25) \wedge (V_{606} - I_{814} > 0.72\,(I_{814} - H_{160}) + 1.3) \wedge (f_u/\mathrm{e}f_u < 2.5) \wedge (4.2 < z_{phot} < 5.5) \wedge (J_{125} < 26.7) \vee (\text{other LBG with } 4.2 < z_{phot} < 5.5)$$

The contamination rates produced by stars, transient objects, lower redshift sources, etc. were estimated by Bouwens et al. (2015). According to their results, the total level of contamination would be around $\sim 2\%$ and $\sim 3\%$ for the $z \sim 4$ and $z \sim 5$ samples, respectively. The major source of contamination would be due to lower redshift sources where the noise in their photometry could perturb the fluxes in a way that satisfies the selection criteria.

From the selection described above, we obtain 5617, 6238, 5859 and 3002 sources at $z = 2,\ 3,\ 4$ and 5. Sources at $z \sim 2$ and 3 where then cross-matched with the detected sources in the 3DHST catalogs, using a minimum separation of 0.25 arcsec, and from that process we obtained a match for 4830 and 4800 at $z \sim 2$ and $z \sim 3$. At $z \sim 4$ and 5 we make an additional cut to our catalogs, selecting only sources with good Spitzer/IRAC photometry extractions. This filtering produces samples of 4125 and 2113 galaxies at $z \sim 4$ and $z \sim 5$.

The redshift distributions of each sample are shown in Figure 1.1, where the redshifts shown correspond to the ones obtained from our SED modeling procedure (see Section 2.1.). The mean redshift of each sample are $\langle z \rangle \sim 1.8, 2.6, 3.9, 5.0$.

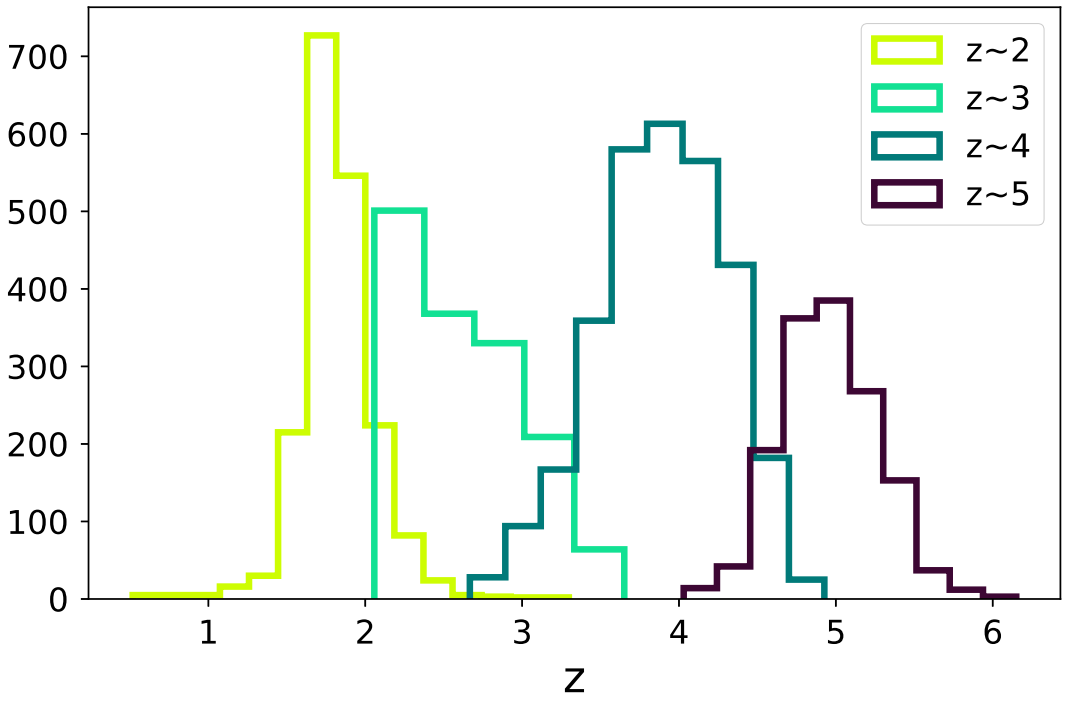

Figure 1.1: Distributions of redshift obtained through SED modeling for each of the selected bins. For the two highest redshift bins $z \sim 4, 5$ bands with potential contribution from nebular emission lines were excluded from this computation, leaving the constraining of the redshift mostly to the rest-frame UV continuum shape.

Chapter 2

SED Modeling

2.1 Fitting Procedure

To obtain our estimates for stellar mass we used an SED fitting method where a set of synthetic spectra is compared to the colors in our galaxies to choose the model that best fit our data. The input models were generated using the single stellar populations (SSPs) of Bruzual and Charlot (2003) and a Chabrier (2003) initial mass function (IMF) with stellar masses between 0.1 and 100 $M_{\odot}$.

An exponentially declining star formation history (SFH) parameterized by the e-folding time τ was used to make composite stellar populations (CSP) with τ in the range $6.5 < \log_{10}(\tau/yr) < 11.0$ in steps of $\Delta \log_{10}(\tau/yr) = 0.1$. Our models had ages ranging from 10 Myr to the age of the universe at each redshift spaced in logarithmic steps of $\Delta \log_{10}(age/yr) = 0.1$.

We chose a single metallicity of $0.2 \times Z_{\odot}$ for all the models. Only weak constraints exist on the Z of galaxies at $z > 3$. This value was chosen motivated by studies like Sommariva et al. (2012) that showed a better agreement of the spectral features of galaxies at $z \gtrsim 3$ when using sub-solar metallicities.

Dust attenuation is applied to all models following the attenuation law described by Calzetti (2011) parameterized by the color excess $E(B-V)$, in the range $0.0 < E(B-V) < 1.0$ in steps of $\Delta E(B-V) = 0.02$. We add redshift as one of the free parameters in the models, and we allowed sources to explore the range $z_{\rm bin} - 1.5 < z < z_{\rm bin} + 1.5$ in steps of $\Delta z = 0.05$ for each of the redshift samples ($z_{\rm bin} = 2,\ 3,\ 4,\ 5$). A summary of the parameters used is shwown in Table 2.1.

The SED fitting was performed using the Python package CIGALE v.2018.0 (Noll et al., 2009; Boquien et al., 2019)[1], that uses a Bayesian-like approach to compute physical properties of galaxies by comparing their photometry to synthetic spectra.

For a set of model parameters $\vec{\theta} = (\tau,$ age, Z, $E(B-V)$, $z)$, a flux $F_{k,\rm mod}(\vec{\theta})$ is computed

[1] https://cigale.lam.fr/

Parameter	Range	Step
Metallicity Z	0.2 $Z_\odot$	fixed
$\log_{10}$(Age/Gyr)	7.0 – 9.5[a]	0.1 dex
$\log_{10}(\tau/yr)$	6.5 – 11.	0.1 dex
$E(B-V)$	0 – 1.0 mag	0.02
R_V	4.05	fixed
z	$(z_{bin}-1.5)$ – $(z_{bin}+1.5)$	0.05

[a] The maximum age is limited by the age of the Universe at the redshift of the source.

Table 2.1: Parameters and their values used to generate our SED models.

by convolving the modeled spectra with the transmission curves of each of the k photometric bands in our catalogs. These modeled fluxes are then compared to the observed fluxes $F_{k,\mathrm{obs}}$ of a galaxy through the χ^2 function,

$$\chi^2(\hat{N},\vec{\theta}) = \sum_{k}^{N_{\mathrm{filters}}} \frac{(\hat{N}\times F_{k,\mathrm{mod}}(\vec{\theta}) - F_{k,\mathrm{obs}})^2}{\sigma_k^2}$$

where N_{filters} is the number of filters in our catalogs and $\hat{N}$ is a normalization between each model and the data. For each model we minimize over $\hat{N}$ and get a likelihood estimation from the resulting χ^2 following $\mathcal{L}(\vec{\theta}) \propto \exp\left(-\frac{1}{2}\chi^2(\vec{\theta})\right)$. A stellar mass and SFR are associated to each model and these values are scaled by the normalization to represent those of our galaxies.

Finally, marginal values for each model parameter and their uncertainties are calculated as the likelihood-weighted means and standard deviations of the parameters in the model grid. For a parameter x, this correspond to:

$$\langle x\rangle = \frac{\sum_{\mathrm{i}} \mathcal{L}(x_{\mathrm{i}})x_{\mathrm{i}}}{\sum_{\mathrm{i}} \mathcal{L}(x_{\mathrm{i}})}$$

$$\sigma_x = \sqrt{\frac{\sum_{\mathrm{i}} \mathcal{L}(x_{\mathrm{i}})(x_{\mathrm{i}} - \langle x\rangle)^2}{\sum_{\mathrm{i}} \mathcal{L}(x_{\mathrm{i}})}}$$

Prior information in this case is given by the range of parameter values in our model grid. Evenly spaced parameters correspond to a flat prior. We will refer to these values as the *Bayesian estimates*. On the other hand, to the set of parameter values that result in the minimum χ^2 (or the maximum likelihood) value we will refer to as the *maximum likelihood estimates* (MLE) from here on.

2.1.1 Maximum Likelihood vs Bayesian Stellar Masses

The procedure described above results in a probability distribution for the values of the model parameters. This leads us to the matter of which value to report, since there are multiple statistics to summarize the original distribution. One way of doing it is to report the best-fit values, the set of parameters that minimize χ^2 (or maximize the likelihood). This value by itself doesn't have an uncertainty associated but an estimation can be obtained using Monte Carlo simulations.

Another common alternative is reporting the mean and standard deviation of the marginalized posterior distributions. In this case a marginal posterior distribution is created for every parameter by making likelihood-weighted histograms of the values the parameter can take. When the resulting posterior distributions are gaussians and the priors for all parameters are uniform, then both estimates; the maximum likelihood and the mean of the marginalized distribution, should be the same. This is not always the case, as sometimes the distributions for a certain parameter can have long tails or there could be degeneracies that would lead to posterior distributions with more than one local maxima. In these cases the mean could end up at some value that doesn't have a particularly high probability as shown in some example posterior distributions (Figure 2.1).

Since we can't look at the posterior distribution for each of the galaxies in our samples to ascertain the reliability of our reported values, we take a look at the distribution of offsets between the two estimates. A good agreement between the MLE and the Bayesian estimate is indicative of a reasonably "well behaved" posterior (single peaked, symmetric, etc.; Figure 2.2).

Before comparing our estimates of stellar mass and the rest of the model parameters we filter sources with poor fits by establishing a cut on $\chi^2_{\rm min,red} \leq 2$. We also make cuts in signal to noise at some bands. From this point forward, only galaxies with S/N H_{160}, $J_{125} > 3.5$ and S/N [3.6] > 1 are considered. This cut generates samples of 2748, 2224, 3044 and 1468 galaxies at $z \sim 2,\ 3,\ 4$, and 5, respectively.

Figure 2.3 shows the distribution of differences when comparing our Bayesian estimates and the MLE of the stellar mass. At all redshifts studied, the distribution of offsets seem to be centered around zero, and no clear bias towards higher or lower masses when changing estimates is found. The standard deviation of these distributions is ~ 0.1 dex for all samples. Typical uncertainties for individual estimates of the stellar mass are reported to be about a factor 0.3 dex, in this case the amount of sources with offsets $|\log_{10}(M_{*,\rm bayes}/M_{*,\rm MLE})| \geqslant 0.3$ dex are 215, 118, 228 and 147 for the samples at redshifts $z = 2$, 3, 4, and 5 respectively. These numbers amount to $\sim 10\%$ of each redshift sample. This percentages only get reduced by $\sim 1\%$ when considering sources with S/N [3.6] > 2.

Discrepancies between the estimates are more evident for other parameters of the models. One of the parameters that show the largest discrepancies is star formation rate (SFR). Star formation rates have higher systematic uncertainties than stellar masses; they can easily be a factor $\times 10$. Interestingly, the distribution of their offsets only show SFR differences this large towards one side of the distribution, as shown in Figure 2.4. There is a clear

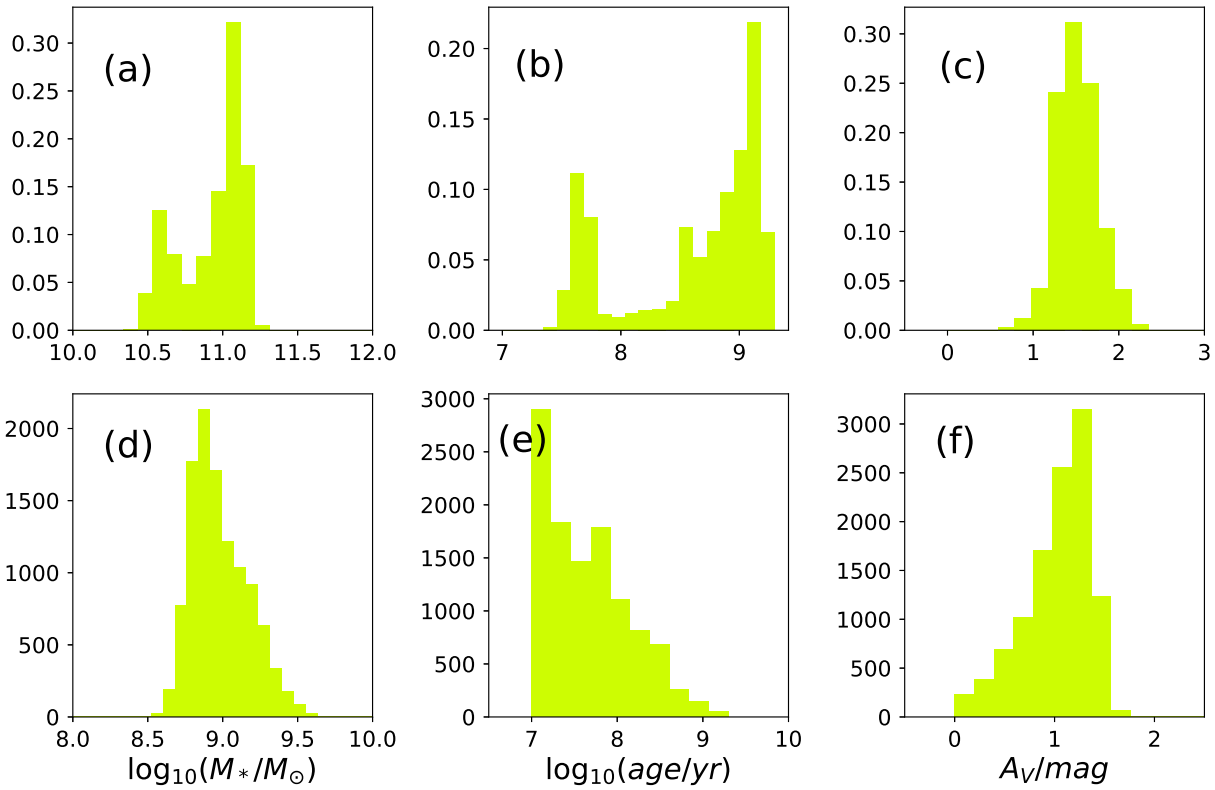

Figure 2.1: Example probability distribution functions for some of the parameters estimated using our chosen SED fitting technique on sources with high stellar mass offsets between the MLE and Bayesian estimates, as indicated in Figure 2.3. From left to right the marginalized posterior distributions for stellar mass, age and extinction in the V band, A_V, are shown. The top row corresponds to a galaxy with multimodal posteriors, where the probability density function (PDF) of stellar mass and age present more than one local maxima. On the lower row the distributions are asymmetrical, which also leads to inconsistencies in the estimated values.

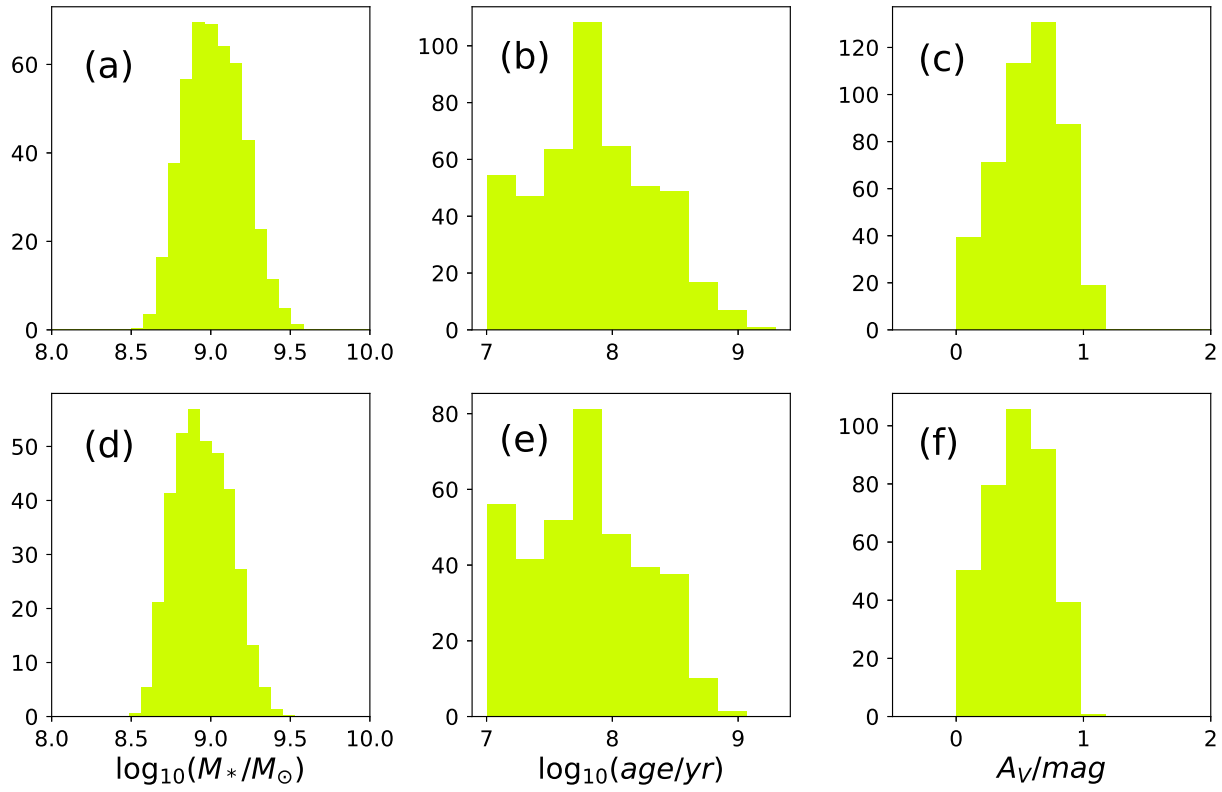

Figure 2.2: Similar to Figure 2.1, the PDFs of stellar mass, age and V-band extinction are shown. Both the source at the top and bottom row have low offsets < 0.3 dex in estimated mass and in this case the marginalized distributions appear more symetric than those shown in Figure 2.1.

set of galaxies that present higher Bayesian SFRs compared to their MLE, even reaching discrepancies as high as $\sim$ 15 dex. In this case the amount of galaxies with offsets $|\log_{10}(SFR_{*,\mathrm{bayes}}/SFR_{*,\mathrm{MLE}})| \geqslant 1$ dex are 999, 616, 1163 and 541 at redshifts $z = 2$, 3, 4 and 5 and they represent a large fraction of each sample corresponding to the $\sim 50\%$, 41%, 38% and 37% respectively.

2.1.2 The Main Sequence of Star Forming Galaxies and its outliers

The main sequence of star forming galaxies is an empirical relation between the stellar mass and star formation rate of star forming galaxies (Noeske et al., 2007). Both of these quantities are related to the mass evolution in a galaxy and they provide measurements of its growth. On the one hand, the SFR indicates the instantaneous assembly of mass, while on the other, the stellar mass quantifies the accumulated growth, so the relation between them is an excellent way to inform models about galaxy evolution and growth.

This relation is well established up to very high redshift and most star forming galaxies fall along this sequence. However, evidence has surfaced questioning the validity of our estimates

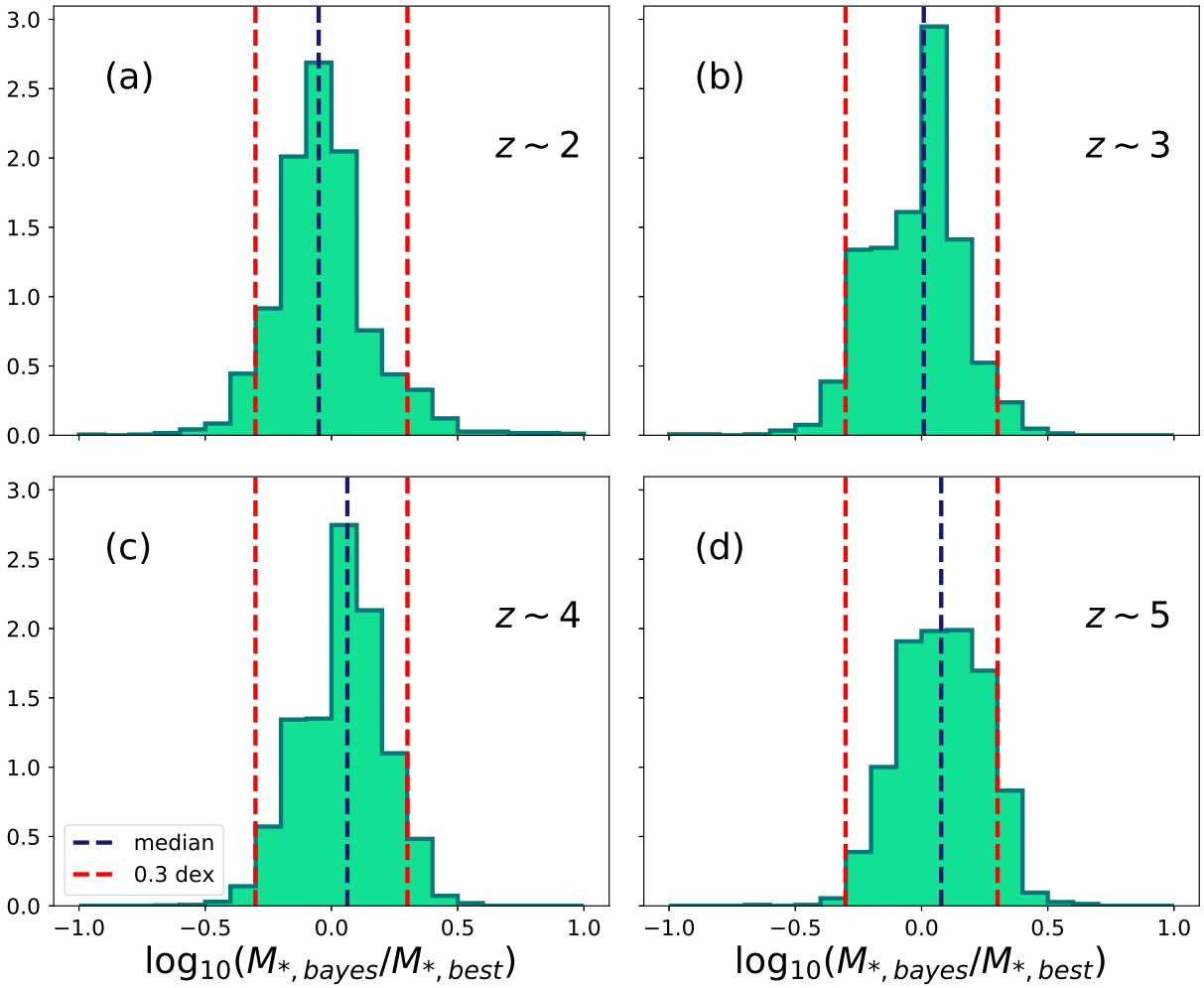

Figure 2.3: Distribution of offsets between Bayesian and MLE estimations of stellar mass for all redshifts studied in this thesis. Vertical dashed blue lines indicate the median of the distributions shown, for all redshifts considered, this value is close to zero. Vertical dashed red lines encase sources with differences lower than a factor $\times 2$. The fraction of the distribution contained inside these lines correspond to $\sim 89\%$, 92%, 93% and 90% at redshifts $z \sim 2$, 3, 4, and 5, respectively.

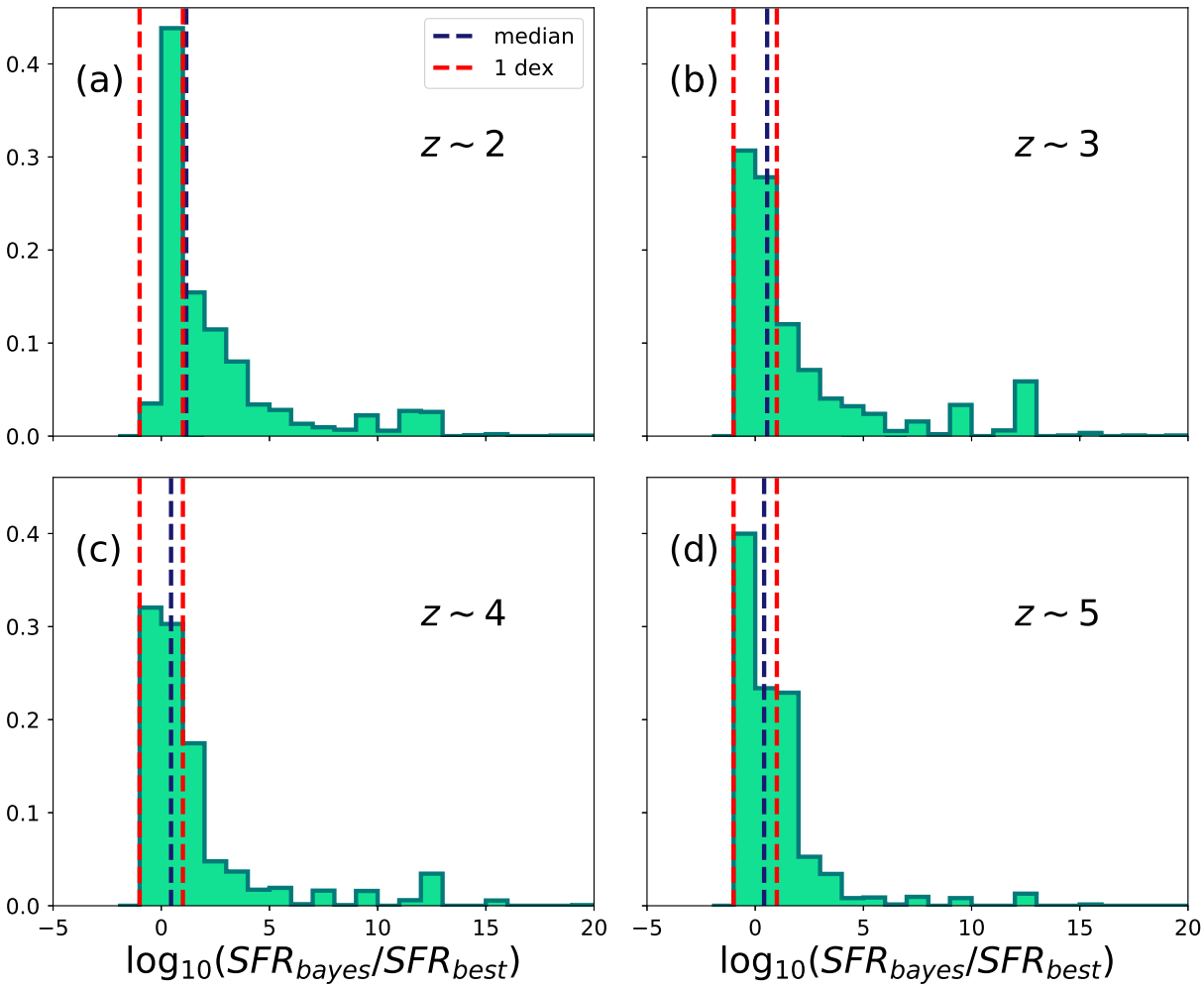

Figure 2.4: Distributions of offsets between Bayesian and MLE estimations of SFR for all redhsifts considered in the study. Dashed blue lines indicate the medians of the distributions with values consistently > 0 at all redshifts. Dashed red lines indicate the -1 and 1 dex limits, representing differences of a factor $\times 10$ in the estimated values. Around a 60% of the samples at each redshift lie inside these limits. All distributions present long tails reaching values of $\log_{10}(SFR_{\rm bayes}/SFR_{\rm best}) \sim 15$ where the MLE model solution is that of a quiescent galaxy.

of stellar mass and SFR at high redshift.

For example, recent studies have shown that typical $z > 2$ galaxies exhibit nebular line ratios (e.g., [O III]/Hα) different to those of local galaxies Shapley et al. (2015), which would suggest that the physical conditions of the ISM are changing at this redshift. There is also evidence of more extreme cases, where a fraction of the population presented high ionization lines (HILs) such as C IV, He II, O III], and C III] in their UV spectrum (Stark et al., 2017; Amorín et al., 2017), lines which are generally not observed in local galaxies of the same M_*.

These galaxies have particularly blue UV colors, enhanced SFR compared to similar mass galaxies (i.e., high specific SFR; sSFR=SFR/M_*) and short ages, with a median of 32 Myr, separating them from the "norma" star forming galaxies in the main sequence. Moreover, the proportion of the population affected by this problem is not minor. Amorín et al. (2017) observed these lines in $\sim 10\%$ of their sample at $z \lesssim 3$.

Trying to model these galaxies using the same assumptions generally used for the "normal" star forming population could lead to erroneus estimates of their physical parameters, and generate artifacts in the distribution of estimated properties of the general population.

As we have estimates of stellar mass and SFR, we explored this relation and studied the effects the choice in reported estimate, MLE or Bayesian, have on its shape. From what we see in Figures 2.3 and 2.4 there are some significant discrepancies in the estimates of stellar mass and SFR and this should have an impact on the shape of the relation between them.

There is a clear difference in the resulting main sequences when using our Bayesian or MLE estimates of stellar mass and SFR as shown in Figure 2.5, where we present the SFR vs. M_* distribution for our sources at $z \sim 4$ (the results are similar at the other redshifts). The main sequence obtained through the Bayesian estimates consist of a single sequence showing a correlation between M_* and SFR. On the other hand, the MLEs show a lot more substructure in the M_*–SFR relation. The spread in SFR is much larger and we have sources with very little star formation, below the main population. These sources would correspond to those at the long tail of offsets in Figure 2.4.

There is also a cluster of highly star forming galaxies, with higher sSFRs, that separates itself from the main population. An interesting feature of this cluster is the accumulation of data points at the top of the distribution. A fraction of the sources in the sample have SFR_{MLE} that correspond to the maximum possible value in our grid of models.

This behavior repeats at all redshifts in our study, and the proportion of the galaxies falling in this cloud of high star formation increases with redshift. This effect is more notorious in the sSFR distribution shown in Figure 2.6. We can see a clear separation of solutions in our samples with a multimodal distribution of sSFR. There is one peak at $\log_{10}(sSFR/yr^{-1}) \sim -9$, corresponding to the main sequence galaxies, and a second one at $\log_{10}(sSFR/yr^{-1}) \sim -7$ corresponding to the outliers.

A similar bimodality has been observed before by Caputi et al. (2017), except that they studied a sample of Hα emmiters at $z \sim 4$–5. They determine empirical separations between the population at $\log_{10}(sSFR) \lesssim -8.05$ and the one at $\log_{10}(sSFR) \gtrsim -7.60$. If we use the

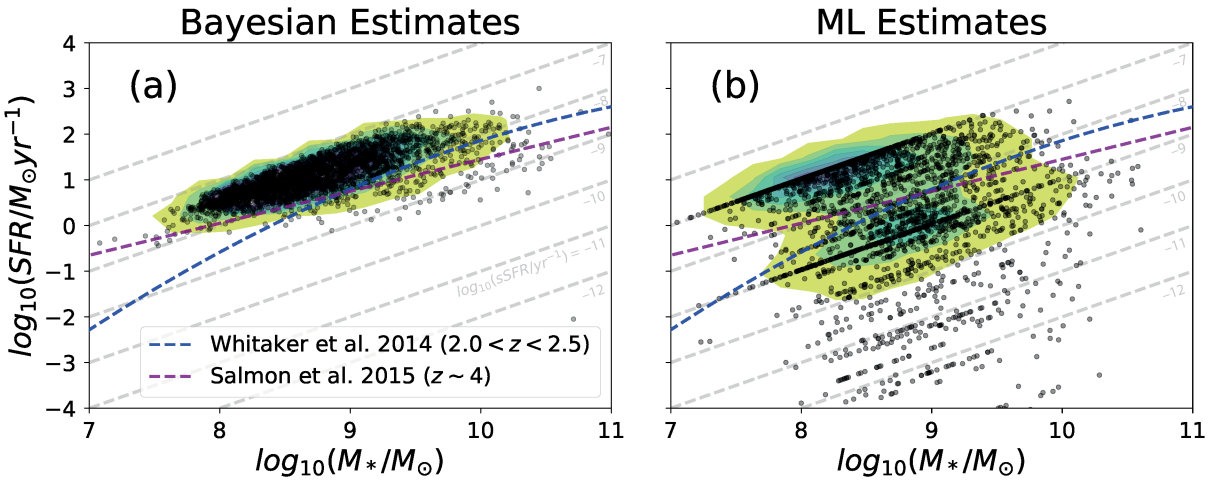

Figure 2.5: Stellar mass M_* vs SFR distributions at redshift $z \sim 4$. The values used in the left panel correspond to the Bayesian estimates while the right panel shows the distributions obtained from the MLEs. In blue, the main sequence relation computed by Whitaker et al. (2014) for sources at $2.0 < z < 2.5$, their highest redshift bin. The increase in SFR at a given M_* shown in panel a) compared to Whitaker et al. (2014) relation is consistent with the redshift evolution of this relationship. Grey dashed lines indicate tracks of constant sSFR.

same criteria to separate our sources we find that the fraction of outliers in our samples are $\sim$ 4%, 38%, 38% and 44% at $z \sim 2$, 3, 4 and 5. These numbers are in agreement with what Caputi et al. (2017) obtain at $z \sim 4$ and 5, where they select a 37–40% of their sample with stellar masses $\log_{10}(M_*/M_\odot) \approx 9$–10.

In trying to understand this bimodality, we explore the other parameters involved in the SED modeling. When we look at the distribution of age and extinction for one of the redshift samples we see very different behaviors for the MLE estimates and the Bayesian ones. The MLE 2D distribution in Figure 2.7 shows two peaks in density, one located close to the youngest allowed age in our models (10 Myr, panel b) and moderate amounts of dust ($A_V \sim 0.5$), and a second one at higher ages (100 Myr) and little to no dust. However the distribution of Bayesian age and dust, displayed in the same figure (panel a), shows a single cloud at intermediate ages and extinctions values (age $\lesssim$ 100 Myr, $A_V \lesssim 0.5$). We identify that the cloud at low ages corresponds to the population of high SFR estimates, in fact, $\sim$ 80% of the sources in this group have a best-fit model with the very-lowest age permitted by our grids (10 Myr), at all redshifts. Sources belonging to this group have posterior distributions like the example shown in Figure 2.1 panel (b), where in some cases a second peak appears at $\log_{10}(age/yr) \sim 8$.

This leads us to believe that the sources that in the MLE appear in the cloud of high SFR, actually have two solutions. They are either very young with high amounts of dust or of moderate ages and lower amounts of dust. This is a known degeneracy of SED modelling when fitting the rest-frame UV and optical, when fitting photometric data (as opposed to spectroscopic).

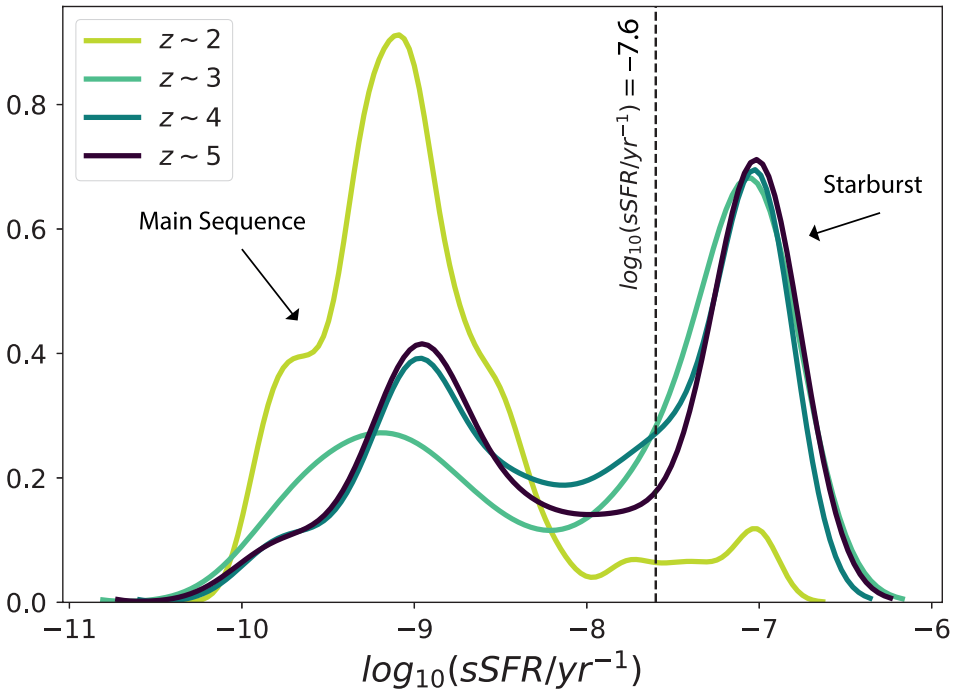

Figure 2.6: Kernel density estimate of the distributions of specific star formation rates for our galaxy populations at each redshift bin. Only star-forming galaxies are considered in this figure, excluding galaxies with $\log_{10}(sSFR) \leq -10$. The vertical black line at -7.6 separates the main sequence sources from the cloud of high SFR as indicated by Caputi et al. (2017).

One way of breaking this degeneracy is to look at the dust emission in the rest-frame IR. The dust around the newly formed stars absorbs a great amount of the flux in the UV range. The absorbed energy ends up being re-radiated in the form of thermal continuum at low temperatures, in the FIR. If we had estimates of the flux being radiated at these long wavelengths we could impose a balance between the amount of attenuation in the UV and the energy re-radiated in the FIR. However, at the redshift of our observations this emission gets pushed all the way to $\lambda > 80$ μm, making it very difficult to obtain detections for individual sources and test if seemingly starbursting galaxies are brighter than the "normal sequence" galaxies in the FIR.

All of this is evidence that the models we are using to estimate the physical properties of these galaxies are not representing them well at these redshifts. These effects, however, are more severe for the estimates of SFR than for stellar mass, as evidenced by the offset distributions of each parameter (Figures 2.3 and 2.4).

2.2 Effects of Nebular Emission

One of the sources of uncertainty in the estimates of stellar mass from broad-band SEDs at high redshift is the contribution of nebular emission. Previous studies have shown that the

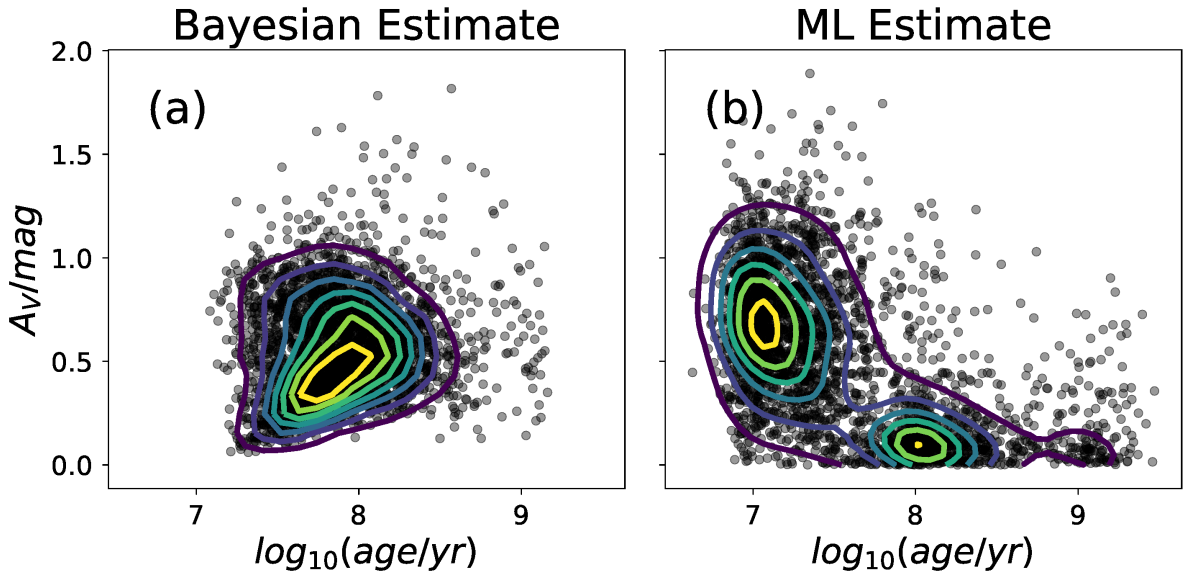

Figure 2.7: 2D distributions of age and dust extinction for the population at $z \sim 4$. Each point represents a galaxy in our catalog, and the contours represent the 2D density levels. On the left panel the estimations used correspond to the Bayesian procedure, while the right panel shows our MLE values for each galaxy. The MLE were perturbed using a normal distribution of size 0.1 for presentation purposes.

contribution of nebular emission to the fluxes of galaxies at high redshift can be significant, altering the estimates of their physical properties (Schaerer and De Barros, 2010). It is important to take these effects into account when we estimate stellar masses.

Nebular emission is produced by the stellar radiation that gets absorbed by the interstellar medium of a galaxy. It consist of two components, continuum emission from free-free, free-bound and two-photon emission, and nebular line emission, constituted mainly from recombination lines and emission from forbidden and fine-structure line transitions. The effect of nebular emission is more prominent at low metallicity and at young ages (Conroy, 2013) where the UV radiation from massive stars gets absorbed by neutral Hydrogen and later re-emitted as a series of lines in the UV, optical and IR. At high redshifts, where the galaxy populations have higher SFRs compared with local galaxies of similar mass, these effects are expected to be significant.

It has been mentioned in previous studies that the added flux from Hα at 6562.8Å could lead to over-estimations of stellar mass as high as a factor of $\times 1.2$ at $z \sim 4$ (Stark et al., 2013), with this effect getting stronger at higher redshift. Recently, studies that rely on estimations of physical parameters derived from broad-band SED fitting have started to add the contribution from these lines into their synthetic spectra Duncan et al. (2014); Song et al. (2016).

The contribution from nebular emission depends on many poorly understood factors, like the metallicity, the escape fraction of photons, the ionizing spectrum of the stellar population, and the gas density of the star forming region. To learn more about these factors, studies

Photometric Band	Emission Line		
	Hβ (4861Å).	[O III] (4959, 5007Å)	$H\alpha$ (6563Å)
IRAC1 [3.6]	$5.4 < z < 7.1$	$5.2 < z < 6.9$	$3.8 < z < 5.0$
IRAC2 [4.5]	$7.0 < z < 9.4$	$6.8 < z < 9.2$	$4.9 < z < 6.7$

Table 2.2: Summary of the emission lines considered for our study of the effects of Nebular Emission on our mass estimates. Indicated are the redshift ranges in which these lines enter the transmission curves of the photometric bands affected at ~ 4, and 5.

of the actual lines and the correlations between their intensities and the physical conditions at high redshift are required. But these lines get redshifted to the MIR, so with the current technology they can not be measured.

Because of the redshift range of our observations, some of the fluxes in our catalogs at $z = 4$ and 5 are potentially contaminated by Nebular Emission lines in the rest-frame optical and we need to take into account these effects when performing estimations of stellar mass. We chose not to add the contribution from emission lines into our SED models to avoid making choices about unknown parameters that could either end up under- or overestimating this effect. Instead, we follow a procedure where we try to estimate directly the offset in mass these lines would produce.

We do this by performing estimations of stellar mass twice for our samples at redshifts $z \sim 4$ and $z \sim 5$, once using all the photometric bands available in our catalogs and a second time leaving out all potentially contaminated bands. When comparing both mass estimates we should see an offset in the retrieved masses produced by the extra flux the emission lines add to the removed bands.

To reduce the amount of factors that can change the resulting masses, we use the same redshift for both estimations. The fit without the contaminated bands is performed first, and in this run redshift is a free parameter of the model. The choice of calculating redshift in the run without contamination was adopted to avoid biases on the redshift estimate due to rest-frame optical emission lines.

We start by identifying the strongest lines that would be present in our samples. The most prominent lines that could appear within the range of our observations are Hα at 6562.8 Å , the [O III] doublet at 4959, 5007 Å and Hβ at 4861.4 Å . The first line to produce contamination is Hα, entering the [3.6] IRAC channel around $z \sim 3.8$ for the $z = 4$ sample. At $z \sim 5$ Hα moves into the [4.5] IRAC channel while [O III] enters [3.6] at $z \sim 5.2$, followed by Hβ, that also enters the [3.6] channel at $z \sim 5.4$. Table 2.2 summarizes the bands and emission lines considered for these experiments, and the ranges of redshift where they may contribute flux to the broadband photometry. An example of the lines in question and their contribution to the fluxes in the [3.6] and [4.5] channels is shown in Figure 2.8, where synthetic spectra with and without emission lines are shown as well as their resulting broad-band fluxes.

For the samples at $z \sim 4$, strong emission lines can only bias our flux measurements for

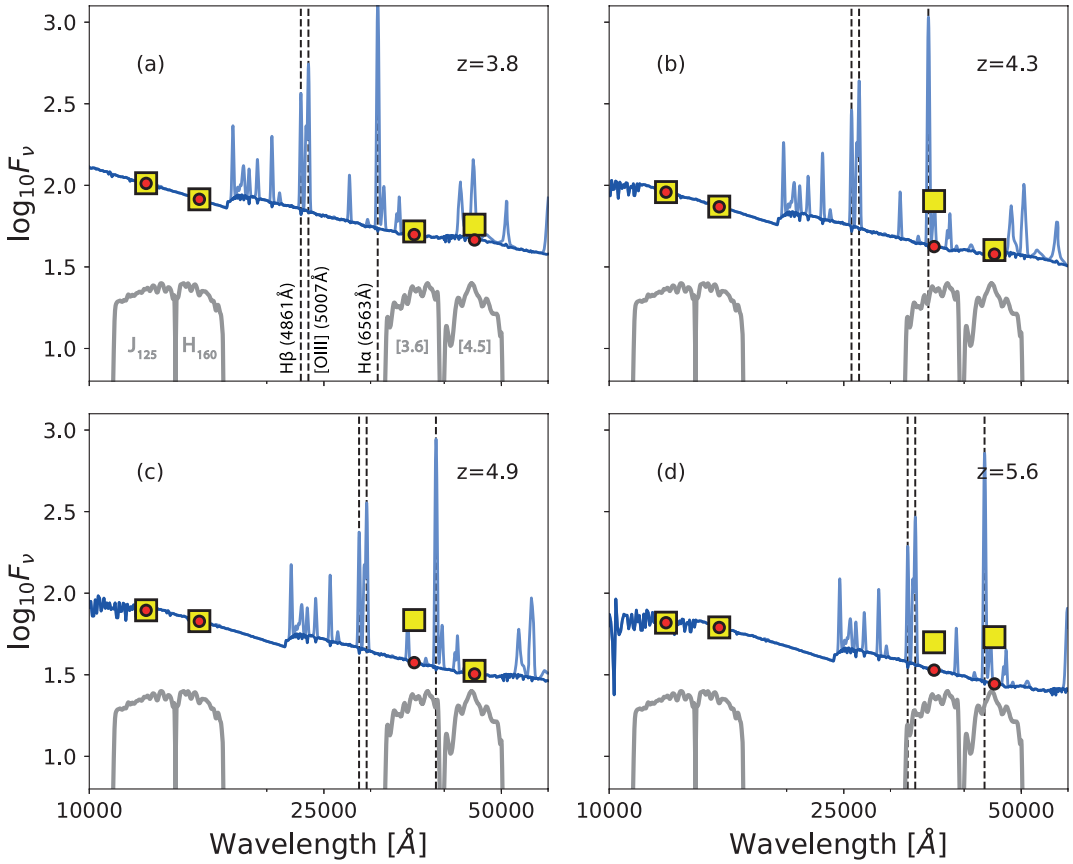

Figure 2.8: Example model SEDs showcasing some of the effects rest-frame optical emission lines have on the integrated fluxes for galaxies at $z \sim 4$, 5.

sources at $z > 3.8$, when the Hα line has entered the [3.6] IRAC channel. We can use galaxies at lower redshifts as a control group an establish an uncontaminated baseline for our stellar mass estimates. To make sure the separation between the contaminated and uncontaminated groups is effective we use information from the full redshift probability density function (PDF) of these sources and only considered sources with at least 1σ confidence of being below or above the limiting redshift. This criteria produces a selection of 976 sources containing flux from nebular lines and 926 sources without, at $z \sim 4$, where cuts for S/N have already been taken into account as described in Section 2.1.

The effects of removing the contaminated bands from the SED fitting are shown in Figure 2.9. In this case the removed band corresponds to the [3.6] IRAC channel. The figure shows histograms for the difference between the masses estimated using only uncontaminated bands (removing [3.6]) and the masses estimated from the whole broadband SEDs available. The distribution in blue corresponds to the control group, where our flux measurements are not biased in any of the cases, and the mass offsets for this sample are distributed around zero, with a mean value of ~ -0.02 dex. As expected, in this case removing photometric bands from the SED fitting procedure doesn't produce an offset in the estimated masses. The discrepancies between the masses is likely caused by the loss in precision given by the lower amount of data points involved in the fitting, but there are no strong biases towards

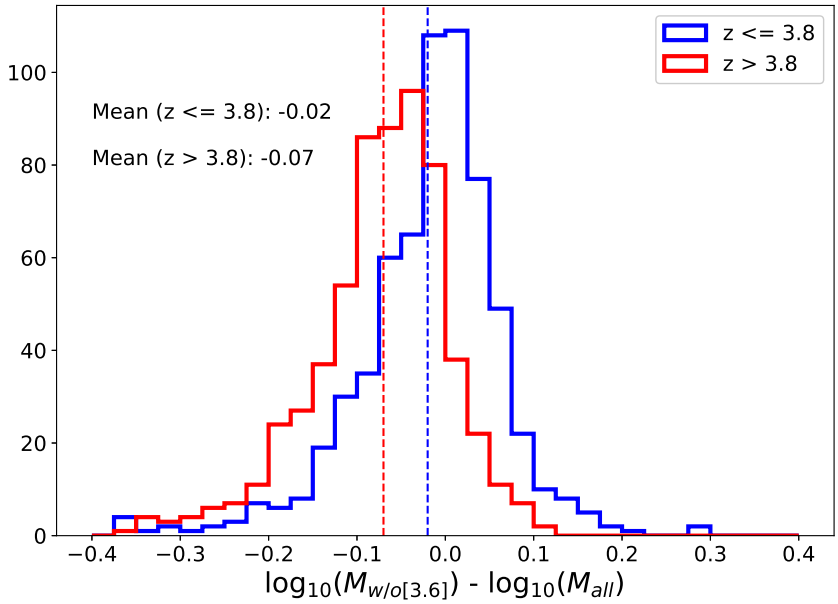

Figure 2.9: Distribution of mass offsets for our sample at $z \sim 4$ from varying the amount of photometric bands included in the SED fitting, as a test of the contribution from nebular emission. The offsets correspond to the difference in estimated Bayesian masses when excluding potentially contaminated bands by emission lines, and using all the available bands. In red the distribution shows the offset in mass caused by the flux contribution from Hα. The distribution in blue is the control group of galaxies with $z < 3.8$, where the flux in [3.6] is not enhanced by any lines. Vertical dashed lines indicate the mean of the distributions, where the control group has an offset of -0.02 dex and the contaminated galaxies, at $z > 3.8$ have a bigger offset of -0.07.

higher or lower masses.

For the case of the contaminated galaxies, in red, their distribution of offsets is centered at a lower value with a mean of ~ -0.07 dex in stellar mass. We can attribute this offset to the excess flux in the [3.6] channel, that, when utilized in the fitting procedure, results in higher estimated stellar masses. It is worth noting that the stellar masses considered in this exercise correspond to the Bayesian estimates from the marginalized distributions.

On the other hand samples at $z \sim 5$ are always contaminated by Hα either at [3.6] or [4.5] and starting at $z = 5.4$ the contribution from [O III] and Hβ is added on top of that. This makes it harder to establish a control group, since for this sample there is not a clear redshift range in which the photometry won't be contaminated. Our strategy then, was to assume that the effects of adding Hα to the [3.6] channel would be replicated when this line entered [4.5] and thus we only needed to figure out the extra offset we would obtain from the contamination of the extra flux when the [O III] and Hβ lines were adding to the [3.6] channel. A separation in our galaxy sample at $z \sim 5$ is then applied and we select galaxies at $z \leq 5.0$ where Hα is within the [3.6] channels transmission curve, and another group at $z > 5.4$ where now [O III] and Hβ are contained in it. This separation yields samples of 418

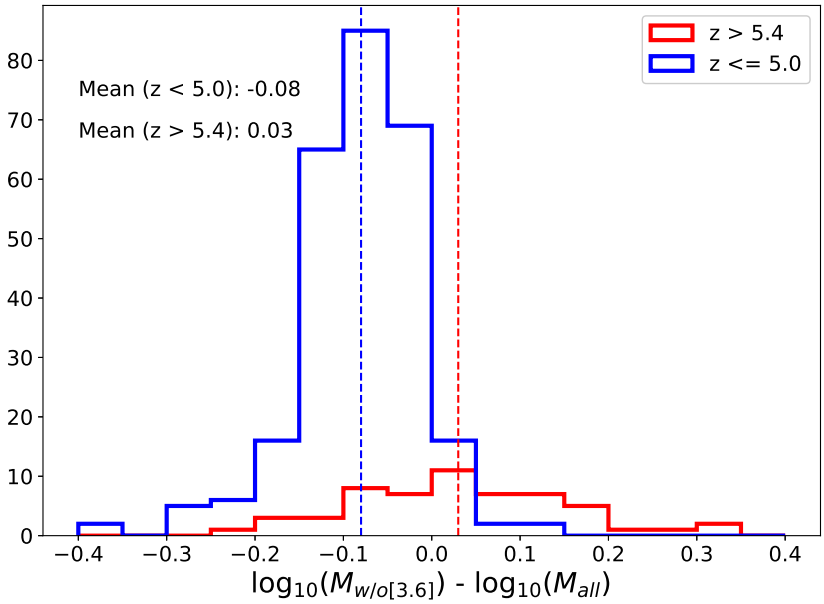

Figure 2.10: Mass offsets for galaxies in the $z \sim 5$ bin. In this case the only band removed from the SED fitting is [3.6]. We separate our sample between galaxies at $z < 5.0$ (in blue), where the contribution of nebular emission lines is restricted to the [3.6] channel. At $z > 5.4$ (in red), Hα has moved to [4.5] and [3.6] has flux contributions from both the [O III] and Hβ lines. The lower redshift sample shows the offsets generated by $H\alpha$, similar to what is shown in Figure 2.9 for the sample at $z > 3.8$. On the other hand, the sample at $z > 5.4$ shows the effect of adding the other two lines to the fitting. Vertical dashed lines of the same colors show the mean of each distribution with values of -0.08 dex and 0.03 dex respectively.

and 80 galaxies respectively.

For our test the only photometric band we remove from the SED fitting procedure at $z \sim 5$ is the [3.6] IRAC channel, since we are interested in establishing the offset in stellar mass the extra contribution of flux from [O III] and Hβ are producing. Figure 2.10 shows the differences in estimated stellar masses at $z \sim 5$ when adding or removing [3.6] to the SED fitting procedure. In blue, the sample of galaxies with redshifts $z \leq 5.0$ are distributed around ~ -0.08, an offset similar to the one the contaminated sample at $z \sim 4$ ($z > 3.8$) showed. This offset shows that the estimated stellar masses that used [3.6] in their fitting are higher by a factor of $\sim \times 1.1$.

On the other hand, the red distribution corresponds to galaxies with $z > 5.4$ where both [3.6] and [4.5] IRAC channels contain nebular emission lines. By removing [3.6] from the fitting in this case, we expect to establish if the addition of the other emission lines, [O III] and Hβ, causes an extra offset in the estimated mass. The distribution of stellar mass offsets has a mean of ~ 0.03 dex, which could indicate that the estimations of stellar mass are not further biased by adding extra flux to [3.6] than what they are from the extra flux at [4.5].

Although there are issues with the SED modeling that lead to major inconsistencies in the

estimates of some of the parameters in our models, stellar masses seem to be robust to most effects. The choice of estimate, between our Bayesian and MLE, only produces discrepancies in estimated stellar masses > 0.3 dex for $\sim 10\%$ of our samples, so the discrepancies for a large amount of our stellar mass estimates are within the typical uncertainties for individual galaxies. Also, since the distribution of offsets between estimates are centered around zero, and don't show evident asymmetries we believe our results for the $\log_{10}(M_*)$–$M_{\rm UV}$ relation are not biased (see Section 3.2). The estimates used from here on correspond to our Bayesian estimates and their associated uncertainties.

Regarding the effects of nebular emission on our masses at $z \sim 4$ and 5, our strategy to study the relation between stellar mass and absolute UV magnitudes is the following. At $z \sim 4$, the sample of galaxies with redshift < 3.8 is unbiased to the effects of nebular lines in all of our photometric bands, so we used our estimates of mass derived using all available bands in our catalogs. For the rest of the sample, whose photometry in the [3.6] channel was contaminated by flux from Hα, we decided to derive stellar mass without using this band, to obtain an unbiased estimate. In that way we used the whole catalog of sources, after our cuts in S/N and $\chi^2_{\rm red}$.

At $z \sim 5$ we use the same approach for the galaxies with $z \leq 5.0$, this sample is only affected by Hα that adds flux into the [3.6] channel, so by removing this band from the SED fitting the estimations of stellar mass at this redshift result unbiased. For the rest of the sample, at $z > 5.4$ the contribution of flux from emission lines occurs in both IRAC channels so to deal with the offsets this produces in mass is harder. There is also a population of galaxies in between that receive contaminating flux in [3.6] only from [O III], since Hβ hasn't entered the band yet. Separating these effects is too difficult and since we have enough sources at $z < 5.0$, we decided to only perform the rest of our study with them.

Chapter 3

The Stellar Mass Functions

Our galaxy stellar mass functions were computed following an approach similar to previous works (González et al., 2011; Song et al., 2016), in which previously computed rest-frame UV luminosity functions are combined with an empirical relationship between M_* and the UV luminosity to transform the UV LF into the GSMFs. We use this method to take advantage of the robustness of the observed UV LFs, which not only reach very faint luminosities, but they are also carefully corrected for many potential biases like selection effects and incompleteness corrections.

An important step in the construction of our GSMFs was to understand the M_*–M_{UV} relation. Not only do we need to establish reliable trends that represent the distribution of stellar mass and UV luminosities, the scatter of the distribution is of particular importance to extend the distribution to lower luminosities and account for the potentially unobserved population of galaxies below our detection threshold.

3.1 Rest Frame UV Luminosity

Because our galaxies span a range of redshifts, they are not all sampled by our filters at exactly the same rest-frame wavelengths. To estimate their UV fluxes always at the same wavelegnth, we estimate the rest-frame UV absolute magnitudes of our galaxies at $\lambda_{\rm rest}$ = 1600 Å, interpolating between all available observations in the UV range. In our interpolation, we modeled the redshifted rest-frame UV SED of each galaxy as a power law of the shape $f_\nu \propto \lambda^\beta$ (Meurer et al., 1999).

To make sure we captured the correct shape of the UV continuum, we only use bands that are unaffected by the Lyman α emission line at $\lambda_{\rm rest} > 1215.6$ Å nor the Balmer jump at $\lambda_{\rm rest} < 3646$ Å. The bands used for each redshift bin are listed in Table 3.1. After that, from the best-fit model we computed rest-frame absolute magnitudes at 1600 Å using the estimates of redshift we recovered from the SED fitting.

To get uncertainties for our rest-frame UV magnitudes we used Monte Carlo simulations

z	Bands used to compute M_{1600}
2	B_{435},V_{606},i_{775}, I_{814},z_{850}
3	V_{606},i_{775}, I_{814},z_{850}, J_{125}
4	i_{775}, I_{814},z_{850}, $Y_{98/105}$, J_{125}
5	z_{850}, $Y_{98/105}$, J_{125}, JH_{140}, H_{160}

Table 3.1: Photometric bands used to compute M_{UV} for all our selected redshift samples.

where we perturbed the photometry and constructed a distribution of the resulting absolute magnitudes. In each of the repetitions we added photometric scatter to the set of observed fluxes assuming a normal distribution for the noise characterized by the error in each observation. We also take into account the uncertainty produced by our redshift estimates by following the same procedure. Our reported absolute UV magnitudes and their associated 1σ uncertainties correspond to the median and standard deviation of the resulting Monte Carlo distributions.

3.2 The $\log_{10}(M_*)$ vs. M_{UV} Relation

With estimates for the rest-frame UV absolute magnitudes and the stellar mass for all galaxies in our samples, we proceed to study the correlation between them. This correlation allows us to transform the UV-LFs into the GSMFs.

At all the redshifts studied in this thesis a clear linear trend is found between the logarithmic stellar mass, $\log_{10}(M_*)$, and absolute UV magnitude, M_{UV}, as shown in Figure 3.1, where the stellar masses used in the distributions presented correspond to our Bayesian mass estimates. This trend becomes more apparent when we look at the median masses per absolute magnitude bin, calculated in bins of 0.5 mag, corresponding to squares in Figure 3.1. Median masses decrease with absolute magnitude and for all but the faintest luminosity bins this decrement seems to follow a constant slope.

At the faintest bins, galaxies have lower S/N in their IRAC photometry than the more luminous sources and so our estimates of mass become less robust. We constructed median flux stacked SEDs for all absolute magnitude bins with more than 5 galaxies and performed the same fitting procedure as described on Section 2.1. The best-fit models and stacked SEDs for all redshift bins are shown in Figure 3.2.

From the stacked SEDs we note that at the brighter end of the distribution ($M_{\mathrm{UV}} < -19.5$) there is a good agreement between the median of the individual masses and masses derived from the stacked photometry but as we go to higher magnitudes discrepancies in the results start to show. We observe that, on average, galaxies at the faintest magnitude bins have higher stellar estimates than the ones for the stacked fluxes. This effect is likely produced by the lower S/N in the IRAC detections of individual galaxies in these M_{UV} bins, which results in overestimations of their stellar masses.

To avoid biased stellar mass estimates due to emission lines, we removed the bands con-

taining emission lines from our SED fitting procedures. For the sample at $z \sim 4$, this means removing the [3.6] channel from the SED fitting for galaxies at $z > 3.8$. For the $z \sim 5$ sample, we removed [3.6] to estimate masses for sources at $z < 5.0$. Galaxies at $z > 5.0$ have both IRAC channels contaminated, and removing them would lead to very uncertain estimates of mass, so we don't use the galaxies in this redshift range for our analysis of the $\log_{10}(M_*)$–$M_{\rm UV}$ relation.

Only galaxies with $> 3\sigma$ fluxes in the [3.6] channel and whose $\chi^2_{\rm red}$ from SED fitting is < 2 were considered to fit our $\log_{10}(M_*)$–$M_{\rm UV}$ relation. We use the entire distribution of individual galaxies instead of the median masses or the masses derived from stacked SEDs to perform the fit. This is important to include information on the intrinsic scatter to make an accurate transformation from UV-LFs to GSMFs. The number of individual sources used is 1891, 1472, 2394 and 348 for redshift bins $z \sim 2,\ 3,\ 4$ and 5 respectively.

To find the best-fit linear relation between $\log(M_*)$ and $M_{\rm UV}$ we used Bayesian inference to obtain posterior distributions for the parameters of a straight line model. We used a model where the errors in $M_{\rm UV}$ and $\log_{10}(M_*)$ are accounted for in the computation of the likelihood. To characterize the underlying distribution of masses we also added a term for the intrinsic scatter. We test two models for the scatter, the first one where the scatter is constant for the full luminosity range, and a second one where the scatter is allowed to vary in a simplified manner.

The resulting likelihood is:

$$\mathcal{L} = \prod_{\rm i=1}^{N_{\rm gal}} (2\pi\sigma_{\rm i}^2)^{-\frac{1}{2}} \exp\left(-\frac{1}{2}\frac{(y_{\rm i} - m x_{\rm i} - b)^2}{\sigma_{\rm i}^2}\right) \tag{3.1}$$

$$\sigma_{\rm i}^2 = \sigma_{M_*,{\rm i}}^2 + m^2\sigma_{M_{\rm UV},{\rm i}}^2 + \sigma_{\rm int,k}^2 \tag{3.2}$$

Were $N_{\rm gal}$ is the number of galaxies in each sample, $x_{\rm i}$ and $y_{\rm i}$ correspond to the absolute UV magnitude and stellar mass of an individual galaxy and m and b are the slope and normalization of our straight line model. $\sigma_{M_*,{\rm i}}$ and $\sigma_{M_{\rm UV},{\rm i}}$ are the uncertainties in stellar mass and absolute magnitude respectively. The term $\sigma_{\rm int,k}$ is the intrinsic scatter for each of the scatter models.

In the first model the scatter remains constant throughout the whole luminosity range, thus $\sigma_{\rm int,1} = \sigma_{const}$, where σ_{const} is a free parameter of the model. The second model considers a change in the intrinsic scatter value at some point in the magnitude range, we parameterize it as follows:

$$\sigma_{\rm int,2}(x) = \begin{cases} \sigma_{\rm bright} & x \leq M_0 \\ \sigma_{\rm faint} & x > M_0 \end{cases} \tag{3.3}$$

This scatter model has three free parameters, the absolute magnitude value where the scatter changes, M_0, and the two values for scatter below and above it, $\sigma_{\rm bright}$ and $\sigma_{\rm faint}$.

To sample the posterior distribution and obtain marginalized distributions for the parameters in this model we use an MCMC algorithm. The sampling was performed using the Affine Invariant Ensemble Sampler (Goodman and Weare, 2010) implemented in the Python package EMCEE (Foreman-Mackey et al., 2013), where an ensemble of random walkers sample the model's probability distribution.

Uniform priors were assigned to each parameter in our model, where the limits for our sampling correspond to:

$$\begin{gathered}
\text{-2.0} < \text{m} < \text{-0.1} \\
-5.0 < b < 5.0 \\
0.0 < (\sigma_{const}, \sigma_{\rm brigth}, \sigma_{\rm faint}) < 10.0 \\
-23.0 < M_0 < -15.0
\end{gathered}$$

The sampling was initialized around a multivariate normal distribution with a width of 10^{-4} for all n dimensions centered at the maximum of the likelihood function.

We used a set of 500 chains that each sampled the posterior distribution for 5000 steps from where 10% of them were discarded as the burn-in phase before constructing the posterior distributions of each parameter. To test the convergence of our chains we computed the autocorrelation time (τ_{ac}) for each of the parameters in our models. For all cases the condition that $100 \times \tau_{ac} < N_{steps}$ was fulfilled, indicating that our chains had enough time to obtain sufficient independent samples.

Our best-fit $\log_{10}(M_*)$–$M_{\rm UV}$ relations are shown as solid red lines in Figure 3.1 and the intrinsic scatter for the distributions, resulting from the single scatter models, is shown by the shaded region. Also shown in the figure is the best-fit trends found by Song et al. (2016) at $z > 4$, who used a combination of median masses and masses from stacked photometry to obtain the trends. Song et al. (2016) uses a Salpeter (1955) IMF so we multiplied their masses by a factor $\times 0.6$ to compare with our estimates which use the Chabrier (2003) IMF. The slopes we find for the $\log_{10}(M_*)$–M_{UV} relation are shallower than those found by Song et al. (2016) at $z > 4$. We obtain values of $m = -0.41$ and $m = -0.35$ at $z \sim 4$ and 5 respectively, while they get steeper values of -0.54 and -0.50 for the same redshifts. We also find shallower slopes than González et al. (2011) who find a slope of -0.68 for their sample at $z \sim 4$.

The best-fit parameters we obtain from our single scatter models are listed in Table 3.2. And from them we can look at the evolution of the trend. Slopes and intrinsic scatter don't show much variation, slopes maintain a value of ~ -0.35 at all redshift except at $z \sim 4$, where we get a steeper trend with a slope of -0.41. In Figure 3.3 we see that the trends at $z \sim 2$, 3 and 5 are almost parallel. The evolution of the normalizations is also noticeable from this figure, and we see how for a given absolute magnitude bin the stellar masses decrease with redshift.

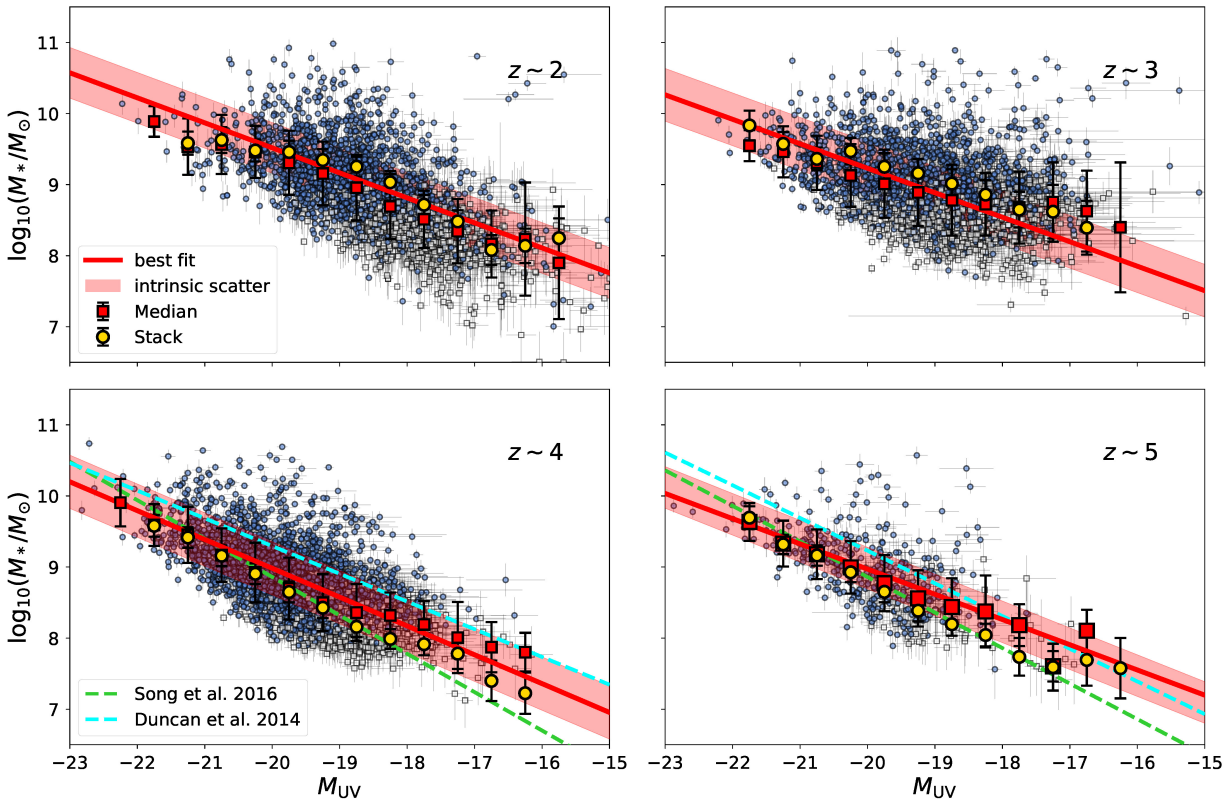

Figure 3.1: Stellar log mass (M_*) vs. rest-frame UV absolute magnitude at 1600Å ($M_{\rm UV}$) distributions for $z = 2$–5. Small blue circles represent individual galaxies in our samples with S/N $\geqslant$ 3 in [3.6] and white squares represent galaxies with S/N $<$ 3. Error bars correspond to the 1σ uncertainties in both estimations of mass and absolute magnitude. Red squares correspond to the median masses in absolute magnitude bins of size 0.5 mag and their respective errorbars represent the standard deviation of the group. In yellow circles the masses derived from stacked photometry in the same magnitude bins is shown. Our best-fit model trends are traced by a solid red line at each redshift, and the shaded red area corresponds to the width of the intrinsic scatter found by our MCMC exploration of parameter space. Also plotted are the best-fit trends from Song et al. (2016) (in dashed green lines) and Duncan et al. (2014) (in cyan dashed lines) at $z \sim 4$ and 5.

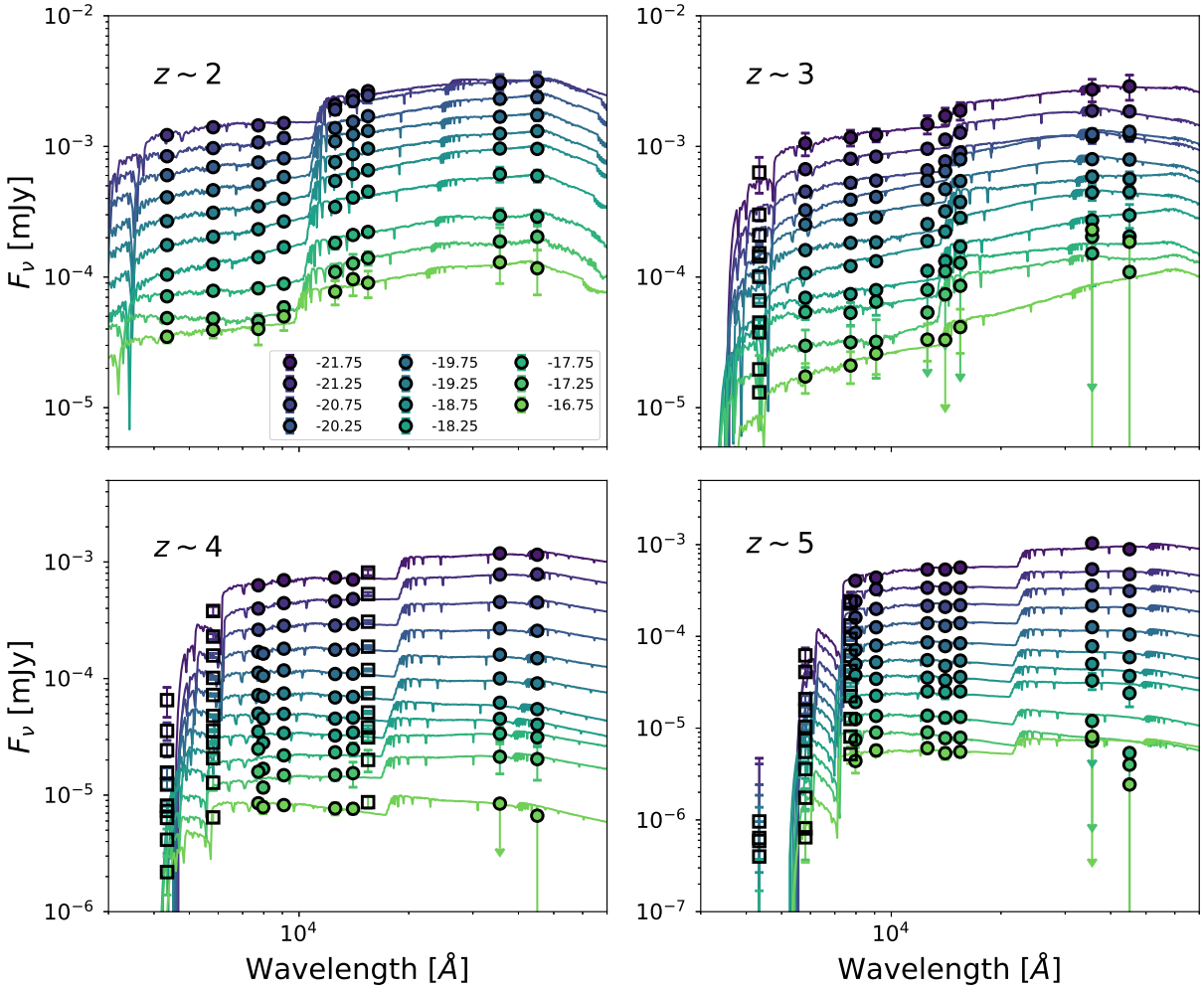

Figure 3.2: Median flux stacked SEDs at $z = 2$–5. Stacks were performed in bins of rest-frame UV magnitude with $\Delta M_{\rm UV} = 0.5$ mag with more than 5 galaxies. The stacked fluxes are represented by filled circles and errorbars corresponding to their 1σ uncertainty. Downward pointing arrows indicate sources with S/N < 2. Unfilled squares correspond to those bands not used in the SED fitting, we leave out all bands bluewards of the Lyman limit, and H_{160} at $z \sim 4$ since in the $3.5 < z < 4.5$ range it is positioned at the Balmer Break ($\lambda_{\rm rest} = 3646$ Å) . The solid lines indicate our best-fit models. Stacked fluxes and models are color-coded by their UV absolute magnitude bins, as indicated in the legend.

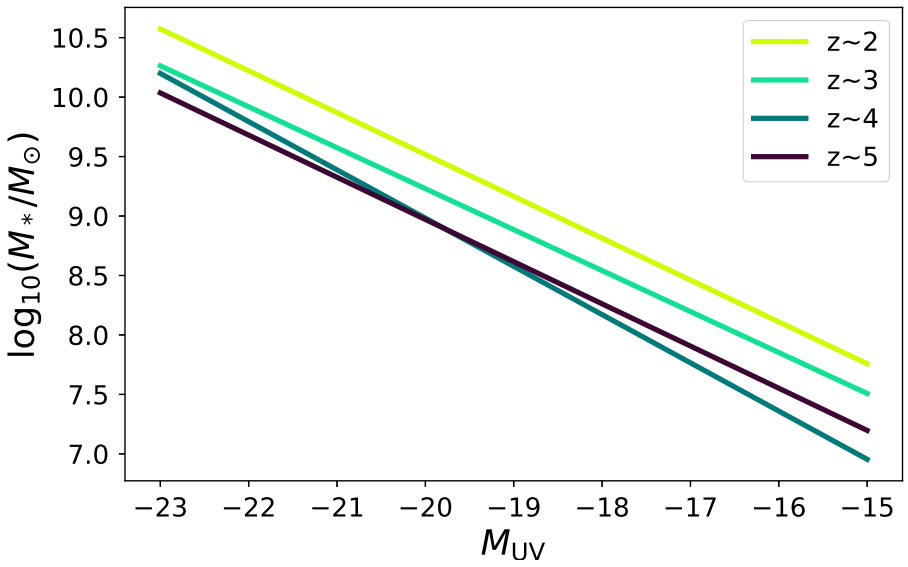

Figure 3.3: All best-fit trends obtained from our model fitting procedure at $z = 2$–5.

Table 3.2: Best fit parameters for $\log_{10}(M_*)$-$M_{\rm UV}$

z	Normalization ($\log_{10} M_\odot$)	Slope	Scatter ($\log_{10} M_\odot$)
2	$2.48^{+0.15}_{-0.15}$	$-0.35^{+0.01}_{-0.01}$	$0.36^{+0.01}_{-0.01}$
3	$2.34^{+0.14}_{-0.14}$	$-0.34^{+0.01}_{-0.01}$	$0.37^{+0.01}_{-0.01}$
4	$0.87^{+0.09}_{-0.09}$	$-0.41^{+0.01}_{-0.01}$	$0.37^{+0.01}_{-0.01}$
5	$1.88^{+0.22}_{-0.24}$	$-0.35^{+0.01}_{-0.01}$	$0.29^{+0.03}_{-0.03}$

One of the advantages of our model is that we get an estimate of the intrinsic scatter from the data itself. Our results yield intrinsic scatters of ~ 0.37 dex for the first three redshifts and a slightly lower scatter at $z = 5$ of ~ 0.3 dex. We can estimate intrinsic scatter from the dispersion and errors in M_* by calculating $M^2_{*,\rm RMS} - \langle\sigma_{M_*}\rangle^2$. For the same sources used in the fit of the M_*–$M_{\rm UV}$ trend we get values of ~ 0.47, 0.43, 0.45 and 0.41 at redshifts $z = 2$, 3, 4 and 5, ~ 0.1 dex higher than our Bayesian intrinsic scatter estimates which consider uncertainty in both $\log_{10}(M_*)$ and $M_{\rm UV}$.

For our model with variable scatter, at the lowest redshift, $z \sim 2$ and $z \sim 3$, the change in scatter occurs at $M_0 = -18.5$ mag. The difference in scatter between the brighter and fainter ends at $z \sim 2$ is about 0.2 dex going from $\sigma_{\rm bright} = 0.36 \pm 0.01$ to $\sigma_{\rm faint} = 0.16 \pm 0.06$. At $z \sim 3$ the difference is also of ~ 0.2 dex, but this time the scatter increases at the fainter end, going from $\sigma_{\rm bright} = 0.37 \pm 0.01$ to $\sigma_{\rm faint} = 0.58 \pm 0.05$. For both samples the scatter at the bright end of the distribution, in this case for sources at $M_{UV} < -18.5$, is consistent with the intrinsic scatter obtained from the single scatter model fit.

At the two highest redshifts, $z \sim 4$ and $z \sim 5$ the change happens around $M_0 \sim -20.3$ mag. For the sample at $z \sim 4$, the difference in scatter is insignificant, going from $\sigma_{\rm bright} = 0.37 \pm 0.04$ to $\sigma_{\rm faint} = 0.38 \pm 0.02$, well within 1σ. At $z \sim 5$, the difference increases to ~ 0.1

dex, with changes from $\sigma_{\rm bright} = 0.23 \pm 0.1$ to $\sigma_{\rm faint} = 0.34 \pm 0.05$.

We performed a model selection analysis using the Bayesian Evidence Z (or sometimes referred to as the *marginal likelihood*), that represents the probability of observing some data given our model. This term is most of the time difficult to calculate, and not always necessary when doing Bayesian inference so it is usually treated as a normalization term for the posterior distribution and doesn't enter the calculations. However, we can get an estimation for this integral using the Dynamic Nested Sampling algorithm implemented in python's package DYNESTY (Speagle, 2019). From this we obtained a Bayes Factor, or odds ratio, between the models evidence at each redshift for the single scatter model compared to the double scatter one. We interpret these results using the scale by Kass and Raferty (1978).

At $z \sim 2$ we obtain a Bayes Factor of $\log_{10} \mathrm{OR}_2 = -4.1$, which would indicate strong support in favor of the varying scatter model. At $z \sim 3$, the Bayes Factor is also negative, supporting the double scatter model but the value is lower. We get $\log_{10} \mathrm{OR}_3 = -0.7$, and this would be in the range of "substantial" support against the single scatter model at $z \sim 3$. At the highest redshift the results are in favor of the single scatter model, but the strength of the support is also lower. At $z \sim 4$, where the scatter barely changed for the higher to the lower masses, the Bayes Factor we obtained is $\log_{10} \mathrm{OR}_4 = 0.99$ which is in the limits of strong support for the simplest model. Lastly, at $z \sim 5$ we have a Bayes Factor of $\log_{10} \mathrm{OR}_5 = 0.35$ that doesn't support strongly either of the models.

From this analysis we only find substantial evidence for varying scatter at the two lowest redshifts, while at the highest redshifts our results don't support strongly any of the models. S/N is similar for [3.6] at all these redshifts, so the varying degrees of confidence in our model selection can't be due to that. As our results don't confidently favor any of the models at all redshifts, we will choose the simplest case and assume a constant scatter throughout absolute magnitudes.

With our estimates for the intrinsic scatter of the relation we can explore the outlier fraction. We find $\sim 35\%$ of the sources at distances $> 1.0\ \sigma_{\rm int}$ from the best-fit relation at each redshift. The distribution of masses for a given absolute magnitude appears skewed to the higher mass end, and most of the more extreme outliers (at distances of $> 2\ \sigma_{\rm int}$ from the best-fit line) are sources with higher masses than the median. These sources have higher M/L ratios than average and they should primarily affect the shape of the high mass end of our GSMFs. If we look at their MLE estimates of sSFR, $\sim 35\%$ of them would classify as what we called outliers of the main sequence (see.2.1.1) at all redshifts in our study except for $z \sim 2$, where only $\sim 10\%$ of them have high enough sSFRs.

On the other hand we don't see a contrasting population of low-mass bright sources, these sources would have lower M/L ratios than average and their presence would affect the shape of the low-mass end slope. The lack of these sources is unlikely to be due to a selection effect, since our sources were selected from LBG criteria which works well for these blue sources. It is also unlikely that it is due to an incompleteness effect, since at those luminosities ($M_{\rm UV} < -21$) and masses these sources should have been detected in our IRAC observations.

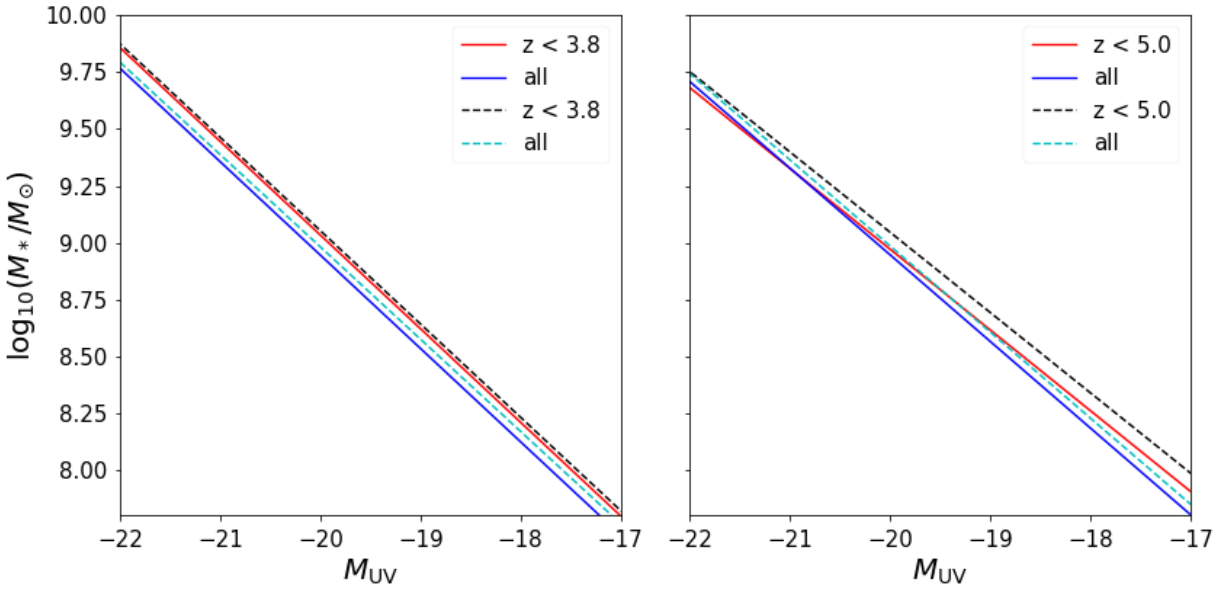

Figure 3.4: Comparison of best-fit trends for $\log_{10} M_*$ and $M_{\rm UV}$ when controlling for nebular emission and not. Dashed lines correspond to the trends obtained from using masses derived from all the available photometry, while solid lines were derived from our estimations of mass corrected by the effects of nebular emission lines. We also show the different trends obtained from using the contaminated sample (in red and black) and the control group (in blue and cyan).

To estimate the offset in the $\log_{10}(M_*)$–$M_{\rm UV}$ trend produced by the nebular emission-contaminated masses, we repeat our line fitting including them. Figure 3.4 shows the results from performing the line-fitting for the stellar mass estimates considering the contaminated bands and not.

At $z \sim 4$, we have two subsamples, one with only those sources without an emission line flux contribution at $z < 3.8$ and the other one that contains all of the sources in this redshift range. For each of these samples we performed the line fitting twice, once using the masses controlling for nebular emission, where we removed the bands with excess flux, shown by the solid lines, and a second one where stellar masses were computed using all available bands in our photometry, in dashed lines. From our results we notice that the slopes for all trends in this redshift range remain the same, the main difference between one set of galaxies and the other is in the normalization. For the uncontaminated sources there is no noticeable offset between the two stellar mass estimates, however for the fit using all sources there is a change in the normalization of 0.1 dex. We see that the trend obtained using the contaminated masses results in higher masses per absolute magnitude bin. Intrinsic scatter increased by ~ 0.01 dex when we used the sample with biased masses.

We can do a similar analysis at $z \sim 5$. In this case there is always a change when using contaminated masses, since there is no control group at this redshift. There is a noticeable difference between the trends for sources with $z < 5.0$, these sources only had contamination in the [3.6] band, so by removing it from the mass estimations we end up with a smaller

normalization (with a difference of ~ 0.1 dex), with lower masses per M_{UV} bin. In this case there is a change in slope when we use the whole sample, resulting in a lower normalization and steeper slope than the sample of galaxies at $z < 5.0$. The biggest discrepancies, in this case, occur at the low mass end of the distribution, in contrast with the case at $z \sim 4$ were all discrepancies were homogeneous in absolute magnitude.

By choosing this approach of removing contaminated photometric bands from our estimations of mass, we obtained trends for the $\log_{10}(M_*)$–$M_{\rm UV}$ relation that won't be biased by the effects of emission lines and consequently won't bias our computations of the GSMFs.

3.3 Galaxy Stellar Mass Functions

The stellar mass functions we constructed are the results of a convolution of previously computed UV Luminosity Functions and our $\log_{10}(M_*) - M_{\rm UV}$ relations at each of the studied redshift selections. Following the procedure described below we take advantage of the robustness of the luminosity functions, where effects like the sample incompleteness due to the survey's depth and biases related to the selection techniques have already been accounted for.

We used the luminosity functions from Bouwens et al. (2019, in prep, private communication), that constructed rest-frame UV-LFs from $z \sim 2$ to $z \sim 9$ using observations from the HUDF, HFF parallel fields and all five CANDELS fields. Their luminosity functions were constructed at $\lambda_{rest} = 1600$ Å going all the way from $M_{1600} \approx -22.5$ to $M_{1600} \approx -16$, and were already corrected for incompleteness and selection effects. Figure 3.5 shows the evolution of these UV-LFs in our redshifts of interest, we are mostly interested in the evolution of the faint-end slope, that gets steeper with redshift, since this will affect the shape of our GSMFs low-mass end slopes.

3.3.1 Computation of the Mass Function

The method used to obtain our GSMFs and their uncertainties is analogous to what González et al. (2011) describe as their "Constant-scatter GSM". This method is devised to correct for the underestimation of the low-mass end slope resulting from the detection limit of the sample. Since the mass-to-light distribution has a non-negligible spread, for a given stellar mass bin there is a distribution of magnitudes in which these galaxies can be detected. At the lowest mass bins of a GSMF this distribution gets truncated by the detection limits of the surveys involved, and a portion of the galaxies belonging to the bin end up not being observed, resulting in a lower number density than expected for the low-mass bins.

One way to correct for this effect is to assume the $\log_{10}(M_*)$–$M_{\rm UV}$ distribution, including its scatter, extends to fainter luminosities. This approach assumes that the distribution of stellar masses at a given absolute magnitude corresponds to a log-normal distribution centered at the best-fit trend for the M_*–$M_{\rm UV}$ relation with a standard deviation equal to

$\log_{10} M_*$ ($M_\odot$)	$\log_{10} \Phi$ ($\mathrm{Mpc}^{-3}\mathrm{dex}^{-}1$)			
	$z \sim 2$	$z \sim 3$	$z \sim 4$	$z \sim 5$
7.25	$-0.93^{+0.11}_{-0.09}$	$-0.85^{+0.11}_{-0.09}$	$-0.83^{+0.12}_{-0.10}$	$-0.89^{+0.19}_{-0.12}$
7.75	$-0.96^{+0.10}_{-0.09}$	$-1.06^{+0.10}_{-0.08}$	$-1.17^{+0.10}_{-0.09}$	$-1.31^{+0.16}_{-0.11}$
8.25	$-1.21^{+0.10}_{-0.08}$	$-1.39^{+0.09}_{-0.07}$	$-1.53^{+0.10}_{-0.08}$	$-1.75^{+0.12}_{-0.10}$
8.75	$-1.52^{+0.08}_{-0.07}$	$-1.76^{+0.08}_{-0.07}$	$-1.91^{+0.09}_{-0.08}$	$-2.24^{+0.11}_{-0.09}$
9.25	$-1.89^{+0.08}_{-0.07}$	$-2.21^{+0.07}_{-0.07}$	$-2.37^{+0.09}_{-0.08}$	$-2.85^{+0.11}_{-0.09}$
9.75	$-2.43^{+0.08}_{-0.07}$	$-2.84^{+0.08}_{-0.07}$	$-2.99^{+0.11}_{-0.09}$	$-3.73^{+0.13}_{-0.10}$
10.25	$-3.25^{+0.10}_{-0.08}$	$-3.77^{+0.10}_{-0.08}$	$-3.85^{+0.13}_{-0.11}$	$-5.06^{+0.18}_{-0.13}$
10.75	$-4.46^{+0.14}_{-0.09}$	$-5.09^{+0.13}_{-0.10}$	$-5.06^{+0.17}_{-0.13}$	$-7.03^{+0.40}_{-0.25}$
11.25	$-6.17^{+0.18}_{-0.12}$	$-6.94^{+0.38}_{-0.25}$	$-6.71^{+0.37}_{-0.24}$	$-10.05^{+0.49}_{-0.25}$

Table 3.3: Galaxy Stellar Mass Functions for all redshifts considered in this study. Lower and upper uncertainties were computed as the 16th and 84th percentiles from the distribution of number density per mass bin.

the intrinsic scatter from our single scatter models (see Section 3.2). This distribution is assumed constant for the whole luminosity range.

We start by sampling the luminosity function in the range $-26 \leqslant M_{\mathrm{UV}} \leqslant -13$, using the best-fit Schechter functions from Bouwens et al. (2019, in prep.) at each redshift. The limits for the sampling were chosen to ensure that the resulting mass functions will be complete in our mass range of interest. We used an importance sampling method to draw $\sim 10^5$ M_{UV} samples in this range, making sure that the whole range is well sampled. We assign stellar masses to each of the M_{UV} values drawn using a log-normal distribution centered at a stellar mass given by the best-fit $\log_{10}(M_*)$–M_{UV} trend and a standard deviation the size of our intrinsic scatter.

To obtain the final number densities for each stellar mass bin we create bins of stellar mass in the range $7.0 < \log_{10}(M_*) < 11.5$, in steps of 0.5 dex and for each bin calculated the number densities. In order to get estimates for the uncertainty of the number densities at each mass bin, we repeated the above procedure 10000 times. For each of these repetitions the luminosity function used was constructed by sampling the posterior distributions of the Schechter parameters Φ^*_{LF}, M^*_{UV} and α_{LF} of the original luminosity function. The GSMFs presented in Table 3.3, correspond to the mean value at each mass bin and the 16th and 84th percentiles of the resulting density distributions. This is represented by red filled circles and vertical lines in Figure 3.6, where our final galaxy stellar mass functions at each redshift bin are shown.

3.3.2 Schechter Fit

We can parameterize our GSMF using a Schechter (Schechter, 1976) function in logarithmic space over mass of the form:

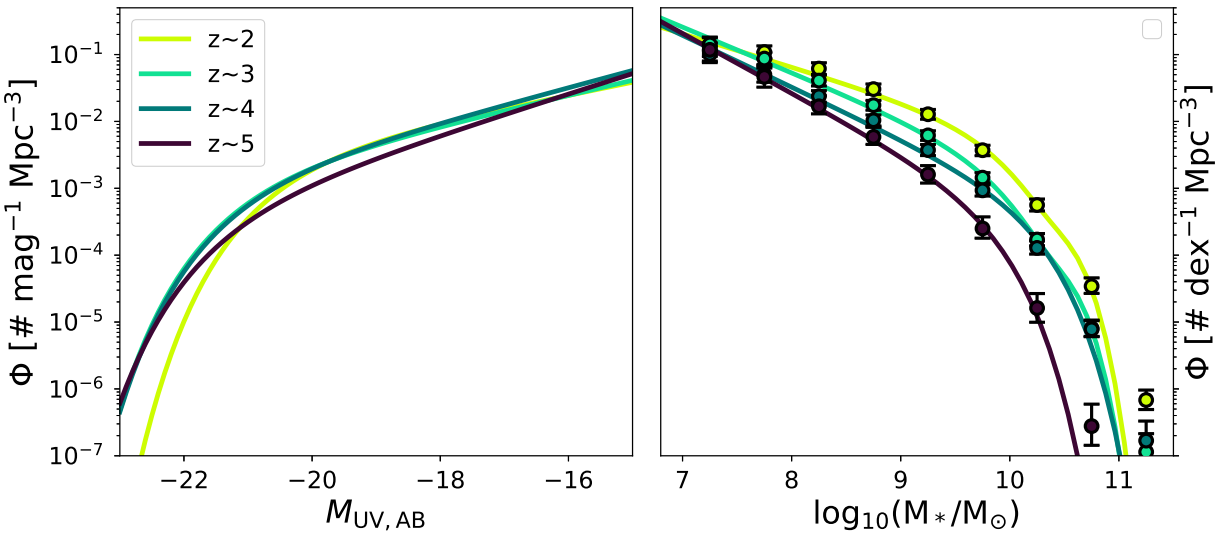

Figure 3.5: Evolution of the UV-LFs used in this study and the resulting GSMFs obtained from them. Solid lines indicate the Schechter fits for both luminosities and stellar masses. Filled circles represent our estimated GSMF and their corresponding 1σ errors.

$$\Phi(M)\mathrm{d}\log M = \ln(10)\Phi^* 10^{(\log M - \log M^*)(\alpha+1)} \exp\left(-10^{\log M - \log M^*}\right) \mathrm{d}\log M, \tag{3.4}$$

This function is defined by a power law at low masses characterized by a slope α and an exponential fall at higher masses. The point of transition between these behaviors is given by the characteristic mass M^* and the function is normalized by Φ^*.

We obtained posterior distributions for these parameters by using an MCMC algorithm analogous to the one used to recover the best-fit parameters for the $\log M_* - M_{\mathrm{UV}}$ trends described in Section 3.2. In this case the likelihood we used to build our posterior samples is analogous to the one described in Section 3.2 but instead of the straight line model we use a Schechter function binned the same way as our GSMFs. Also, in this case the uncertainties considered only take into account the scatter in $\Phi(M)$.

Using EMCEE, we ran an ensemble of 500 chains for 5000 steps each, discarding the first 500 steps as the burn-in phase before constructing the posterior distributions. We explore space linearly for α and logarithmically for M^* and Φ^*, using a uniform prior in the first case and logarithmic priors for the other parameters. The extent of our priors was given by the limits,

$$\begin{gathered} -5 < \alpha < 1 \\ 8 < \log_{10}(M^*/M_\odot) < 12 \\ -10 < \log_{10}(\Phi^*/\mathrm{Mpc}^{-3}) < 0 \end{gathered}$$

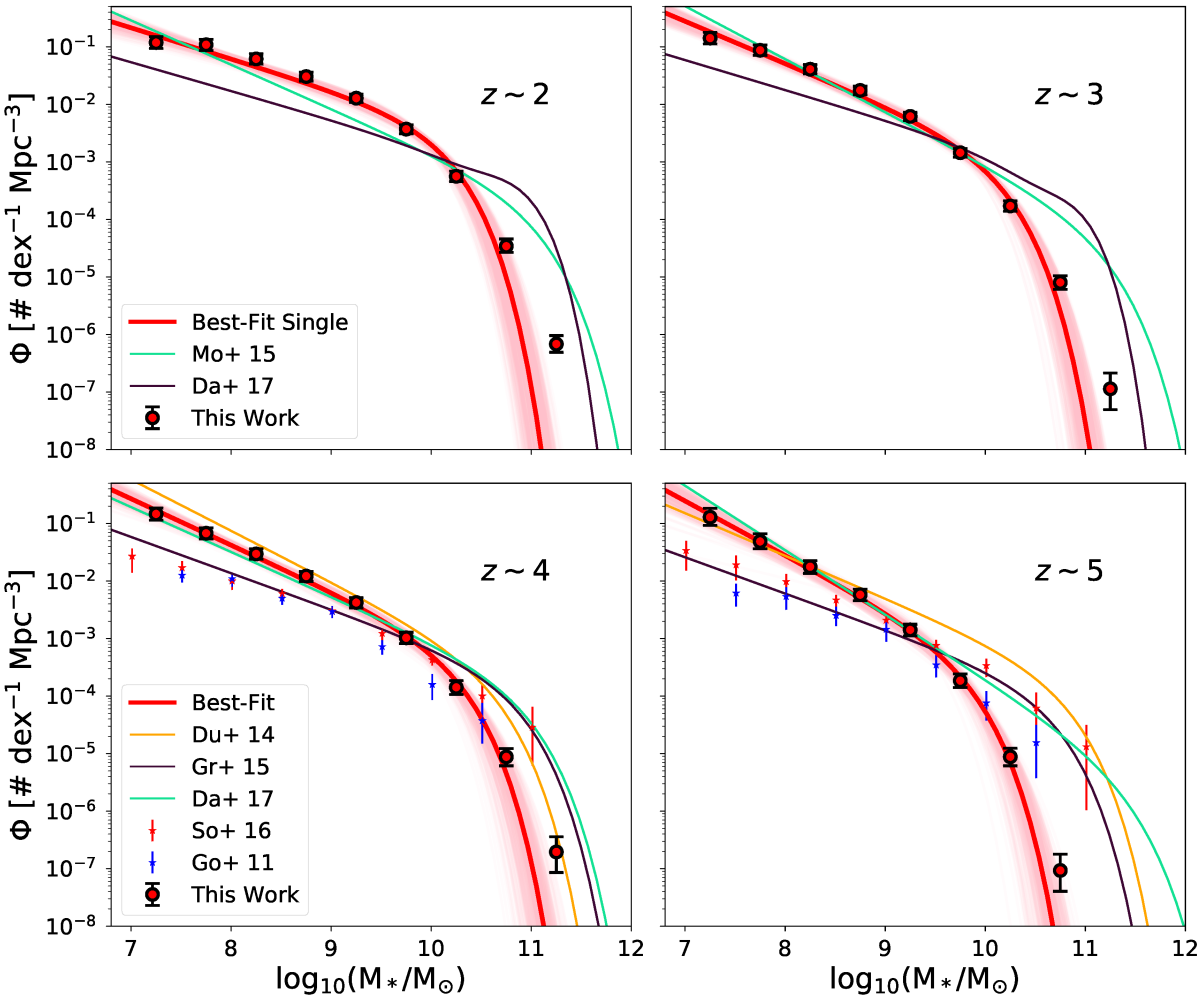

Figure 3.6: Our galaxy stellar mass functions from LBG selected sources at $z = 2$–5 in red filled circles and their respective 1σ errors. The solid red lines represent our best-fit Schechter functions and the light-pink lines correspond to 500 draws from the joint posterior distributions obtained through our MCMC fit. Previously computed GSMF at redshift ranges similar to ours from the literature are plotted beside our mass functions. Mortlock et al. (2015) (Mo+15 in the legend), Davidzon et al. (2017)(Da+17), Duncan et al. (2014)(Du+14), Grazian et al. (2015)(Gr+15), Song et al. (2016)(So+16) and González et al. (2011)(Go+11). Conversion to a Chabrier IMF were applied when needed.

z	$\log_{10}(\Phi^*)$ (Mpc^{-3})	$\log_{10} M^*$ ($M_\odot$)	α	$\log_{10} \rho_*$ ($M_\odot$Mpc^{-3})	$\log_{10} \rho_{*,9.5}$ ($M_\odot$Mpc^{-3})
2	$-2.66^{+0.18}_{-0.17}$	$10.02^{+0.10}_{-0.12}$	$-1.54^{+0.06}_{-0.05}$	$7.58^{+0.04}_{-0.04}$	$7.24^{+0.04}_{-0.04}$
3	$-3.13^{+0.20}_{-0.17}$	$10.02^{+0.20}_{-0.17}$	$-1.73^{+0.06}_{-0.05}$	$7.25^{+0.04}_{-0.04}$	$6.79^{+0.04}_{-0.04}$
4	$-3.46^{+0.21}_{-0.19}$	$10.14^{+0.10}_{-0.14}$	$-1.80^{+0.06}_{-0.05}$	$7.11^{+0.04}_{-0.04}$	$6.67^{+0.06}_{-0.06}$
5	$-3.52^{+0.22}_{-0.23}$	$9.71^{+0.10}_{-0.11}$	$-1.94^{+0.09}_{-0.08}$	$6.66^{+0.06}_{-0.06}$	$5.82^{+0.7}_{-0.08}$

Table 3.4: Best-fit Schechter parameters and their 1σ uncertainties for our GSMFs at $z = 2$–5.

The starting point of each chain was initialized around a multivariate Gaussian centered at the maximum of the likelihood function. We checked the convergence of our chains by computing the autocorrelation time, and for all parameters explored the criteria $100 \times \tau_{ac} < N_{steps}$ was met.

From the resulting joint distribution we obtained the marginalized posteriors for each of the parameters. The mean and the 68% confidence intervals for each of the marginalized parameters in the models are listed in Table 3.4 and were obtained from the marginal posterior distributions as the mean and the 16th and 84th percentiles of each distribution.

Figure 3.6 shows the best-fit Schechter parameterization for all the redshift bins in our study along with a random sample of 500 GSMFs from the joint posterior of Schechter parameters. We compare our GSMFs with recent works at the same redshift ranges (e.g. Mortlock et al. 2015; Davidzon et al. 2017; Duncan et al. 2014; Grazian et al. 2015; Song et al. 2016; González et al. 2011).

The most noticeable disagreement between our GSMFs and those from the literature occurs at the high-mass regime, where we consistently obtained lower characteristic masses than those from the literature, and this discrepancy appears at all redshifts. This could be a selection effect. Our LBG selected galaxies could be biased against passive galaxies with high M/L ratios. Not including these galaxies in our computation of the GSMFs would end up under-predicting the number density of high mass galaxies and we would obtain an exponential fall at comparatively lower stellar masses.

Another factor that could cause an underestimation of the high-mass density would be our method of convolving the parent luminosity functions with our $\log_{10}(M_*)$–$M_{\rm UV}$ distributions. Using a constant scatter means that we do not account for the high-mass outliers we see in our distributions of $\log_{10}(M_*)$–$M_{\rm UV}$. This effect is shown by Song et al. (2016), where a clear discrepancy at the high-mass end of their "Raw Bootstrapped GSMF", that uses the complete distribution of galaxies to convolve samples, and their "Constant Scatter GSMFs" occurs.

At the low-mass end, where our GSMFs are more robust against incompleteness, we find that at $z \sim 2$ our results for the slope agree with those of Davidzon et al. (2017), however there is an offset of ~ 0.7 dex in the normalization, where we produce a higher amount of galaxies at the low mass range. Mortlock et al. (2015) obtain steeper slopes than us at both $z \sim 2$ and 3. They obtain values of -1.74 for their sample at $1.5 < z < 2.0$ and -1.92 at $2.5 < z < 3.0$, compared to our -1.54 and -1.73 slopes at $z \sim 2$ and 3. But it is harder to compare our results at these two redshifts since the selection, construction of the GSMFs, and redshift distributions are different.

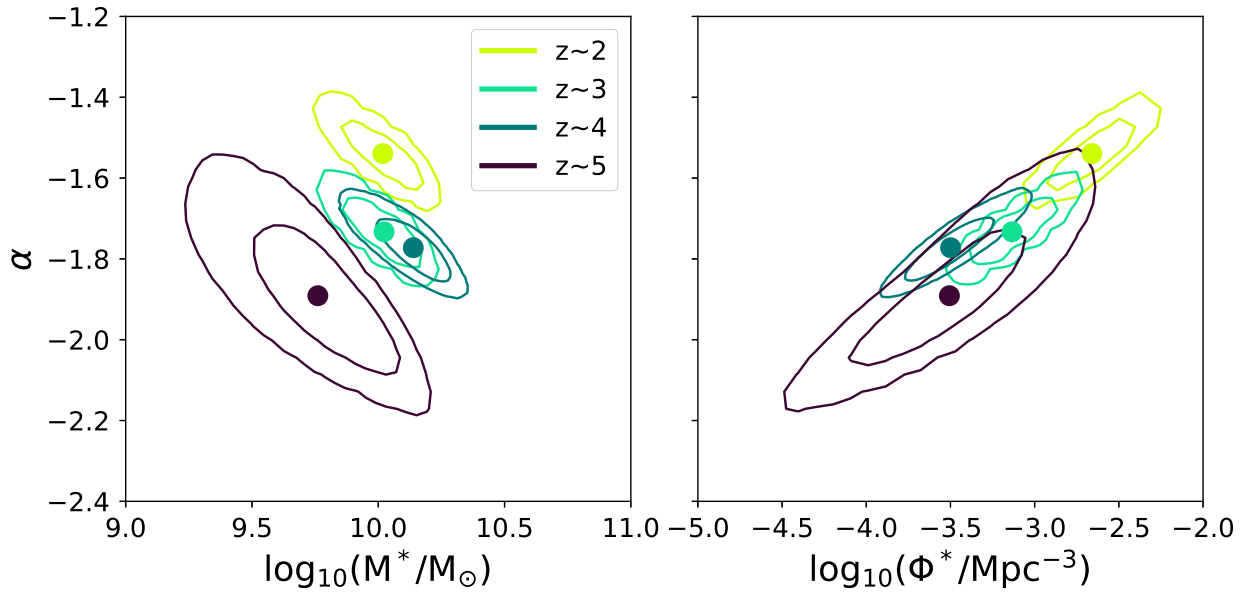

Figure 3.7: Confidence contours of the best-fit Schechter parameters for our GSMFs at $z = 2$–5 at the 68% and 95% levels.

At the highest redshifts, we have the deepest Spitzer/IRAC data from our samples, and so our estimations of stellar mass up to $\sim 10^7 M_\odot$ should be reliable. Of all the works we are comparing with, the ones that reach the lowest stellar masses in their computations are González et al. (2011), Duncan et al. (2014) and most recently Song et al. (2016) so we will focus our comparisons of the low-mass end slope with them.

We have consistently steeper slopes than González et al. (2011) and Song et al. (2016) at both redshifts and compared to the results from Duncan et al. (2014) our slopes are shallower at $z \sim 4$ but steeper at $z \sim 5$. Both González et al. (2011) and Song et al. (2016) construct their GSMFs by combining a UV-LF with a distribution of M_*–$M_{\rm UV}$, so differences in either of the two would have an impact on the extent of our discrepancies. Song et al. (2016) discusses in their work that for a given number density of galaxies in a luminosity bin Φ_L, the $\log_{10}(M_*)$–$M_{\rm UV}$ relation has a direct effect on the number density of galaxies at a mass bin Φ_M, following $\Phi_M \propto \Phi_L(\mathrm{d}L/\mathrm{d}M)$. This would mean that shallower mass-to-light trends would produce steeper GSMF low-mass end slopes. That is the case for our trends compared to Song et al. (2016), as it is shown in Figure 3.1. Something similar happens with the sample from Duncan et al. (2014). Since their slopes for the $\log_{10} M_*$–$M_{\rm UV}$ are shallower than ours at $z \sim 4$, but are in agreement with what we found at $z \sim 5$.

The other factor that could cause discrepancies is the faint-end slope of the luminosity functions used to obtain samples. Song et al. (2016) uses the UV luminosity functions from Finkelstein et al. (2015) who report faint-end slopes of $\alpha = -1.56$ at $z \sim 4$ and $\alpha = -1.67$ at $z \sim 5$. These are shallower than the ones we use from Bouwens et al. (2019, in prep), with values of -1.70 and -1.75 respectively.

From their 2D joint distributions, displayed in Figure 3.7, we can see the correlations between the Schechter parameters as shown by their 68% and 95% confidence contours. The

low-mass end slope correlates both with the normalization and the characteristic mass and these correlations hold at all redshifts in our study. The low-mass end slope α shows a negative and positive correlation with the characteristic mass, M^*, and the normalization factor, Φ^*, respectively.

The 2D joint distribution also shows that the characteristic mass M^* doesn't evolve significantly between $z \sim 2$ to $z \sim 5$, our estimates of M^* are consistent within the uncertainties at all redshifts, and no clear evolution is observed.

On the other hand, both the normalization Φ^* and the low-mass end slope α seem to evolve. This is more apparent in Figures 3.7 (a) and 3.8 (a) and (c), where we see a steepening of the low-mass end slope with increasing redshift and a decrease in normalization. We fit this trend and find a parameterization on the evolution of the normalization,

$$\log_{10}(\Phi^*/\mathrm{Mpc}^{-3}) = (-2.13 \pm 0.05) - (0.30 \pm 0.044)\,\mathrm{z},$$

and the low-mass end slope,

$$\alpha = -(1.31 \pm 0.004) - (0.13 \pm 0.003)\,z.$$

In general this evolution of the parameters is supported by previous studies (e.g., Marchesini et al., 2009; Song et al., 2016) that find that the characteristic mass remains unchanged throughout cosmic time and that the normalization evolves. Our results are qualitatively consistent with the evolution in these studies but we differ in the actual values of M^*.

As we mentioned before, the evolution of the low-mass end slope is a topic of controversy, since there are multiple studies, at all redshifts, both supporting Ilbert et al. (2013); Santini et al. (2012); Song et al. (2016) and disregarding Marchesini et al. (2009); Duncan et al. (2014); Grazian et al. (2015) an evolution of this parameter of the GSMF. What we observe from our results is a steepening of the low-mass end slope from $z \sim 2$ to $z \sim 5$. This is illustrated in Figure 3.9 where our estimates of α are compared to results from the literature. The only other study that uses a consistent method to estimate the GSMFs in the range $2 < z < 5$ is Davidzon et al. (2017), so their results are good comparison point to look at the evolution of α. They find a faster steepening of the low-mass end slope, starting from shallower slopes than us at $z \sim 1$ and ending up with a steeper low-mass end slope than our estimate of $\alpha = -1.89$ at $z \sim 5$. The methodology used to create the mass functions in this study is different than ours and their computations of the GSMF only reaches masses of $\sim 10^{9.5} M_\odot$ at their highest redshifts ($3 < z < 5$), so we consider our estimates in this range more robust.

3.4 Stellar Mass Densities

We can integrate our GSMF to obtain stellar mass density (SMD) estimates at each of the redshifts we studied. This was done by integrating the best-fit Schechter functions recovered from our Bayesian inference analysis. The limits for this integration were chosen between

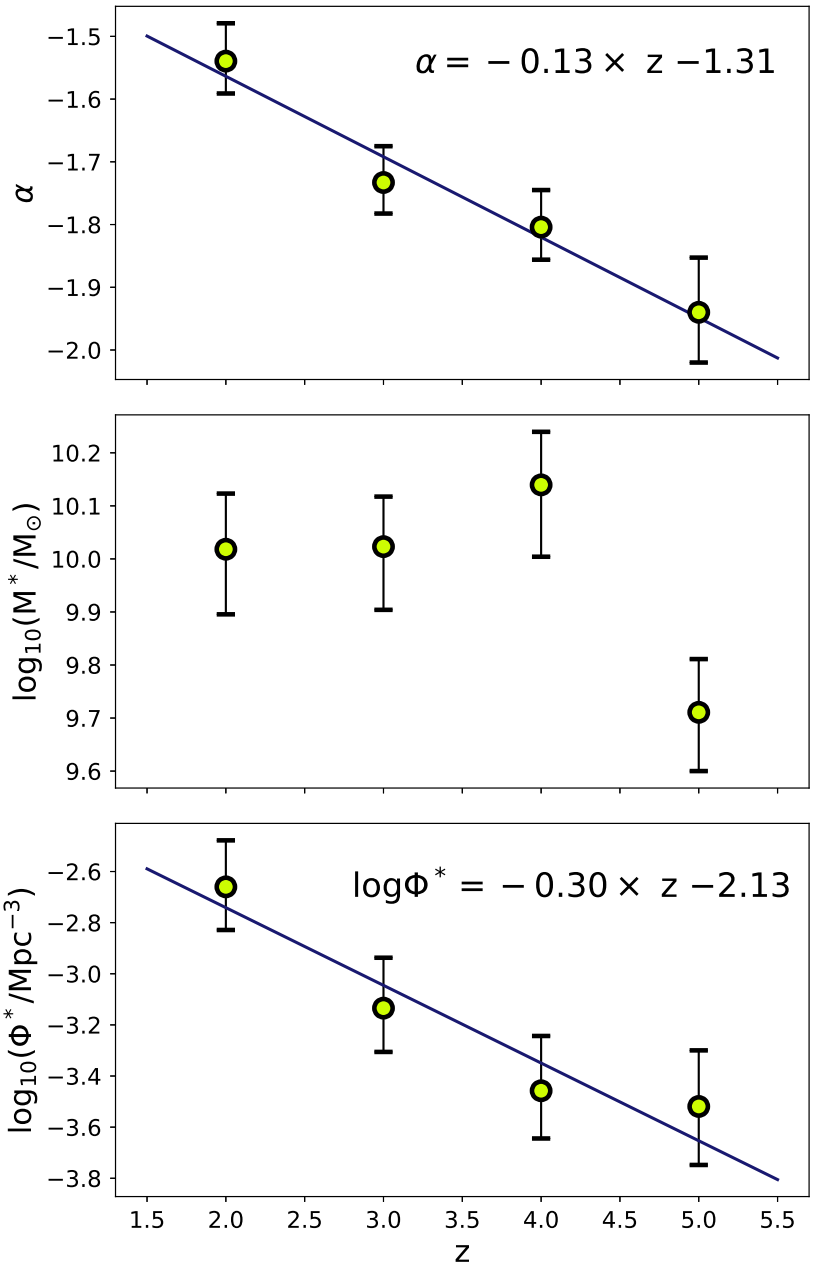

Figure 3.8: Redshift evolution of the best-fit Schechter parameters for our GSMFs. Lower and upper uncertainties correspond to the 16th and 84th percentiles from the posterior distributions obtained from our MCMC fitting. A linear trend is fitted for the evolutions of Φ^* and α with redshift in blue.

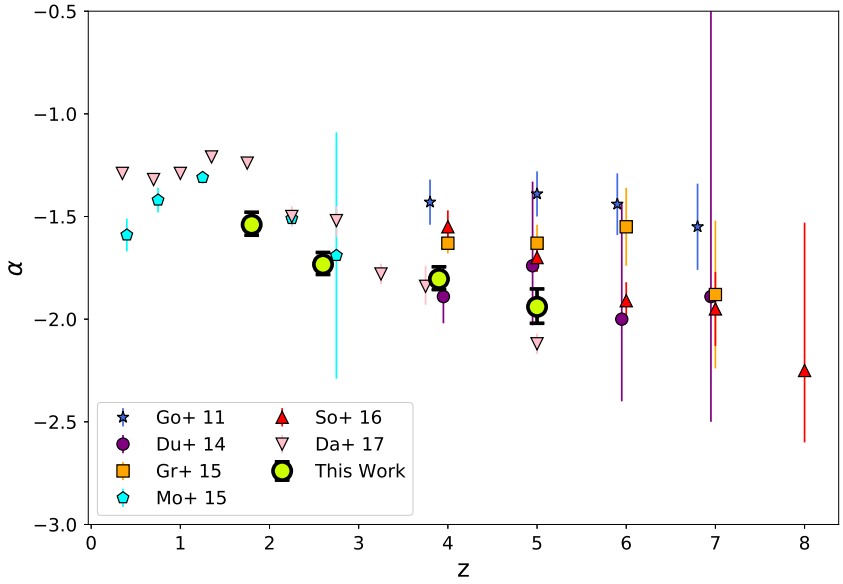

Figure 3.9: Evolution of the Schechter parameter α, the low-mass end slope for our GSMFs (yellow circles). Beside them, previous estimates from the literature are shown.

$8 < \log_{10}(M_*/M_\odot) < 13$, a range often used in the literature that we use to facilitate comparisons with results from other studies. Another way of choosing the value for the low-mass integration limit would be motivated by studies of SFRD. According to Madau and Dickinson (2014) an analogous value to the cut in luminosity functions regularly used, $L_{min} = 0.03L_*$, would correspond to $M_{min} \approx 10^{9.5} M_\odot$. Madau and Dickinson (2014) also mention that SMD estimations are not as sensitive as their SFRD counterparts to the lower integration limit, since GSMFs have shallower slopes than UV-LFs.

Table 3.4 lists our results for the SMD estimates and their 1σ uncertainties calculated by repeating the SMD computation 10^4 times for a different set of Schechter parameters drawn from the joint posterior distributions shown in Figure 3.7. We also computed SMD using the low-mass integration limit $\log_{10} M_* = 9.5$, and we find that the SMDs produced by this choice are ~ 0.4 dex lower at redshifts $z \sim 2$, 3 and 4. The difference at $z \sim 5$ is more pronounced and the change in integration limit produces a SMD 0.8 dex lower. This effect shows clearly that the low-mass galaxies are making a big contribution to the global mass at these redshifts, and this becomes more noticeable at our highest redshift where we obtain the steepest low-mass end slope.

Our results for the evolution of the SMD are displayed in Figure 3.10, together with values from the literature at various other redshifts. The majority of the results presented were taken from the compilation by Madau and Dickinson (2014). We also add results from more recent studies at both low (Mortlock et al., 2015; Davidzon et al., 2017) and high redshift (Duncan et al., 2014; Grazian et al., 2015; Song et al., 2016), converted to a Chabrier IMF when necessary.

In general, our results for the SMDs at $z = 2$, 3, 4 and 5 are in good agreement with previous estimates from the literature. We find similar results to the stellar mass densities

reported by (Davidzon et al., 2017) at our two lowest redshifts $z = 2$ and $z = 3$, but our estimate at $z \sim 4$ is slightly higher than theirs by ~ 0.1 dex. At our highest redshifts $z \sim 4$ and $z \sim 5$ our results are within 1σ of the values obtained by both Song et al. (2016) and Grazian et al. (2015), despite the differences in the shapes of our GSMFs. The shallower low-mass end slopes in their galaxy stellar mass functions get compensated by our lower mass exponential cutoff.

Especially large discrepancies are found between our estimates at $z \sim 4$ and 5 with the results from Duncan et al. (2014), that obtain higher SMDs by ~ 0.5 dex than ours in this range. This offset is explained by the fact that their GSMFs have both steeper low-mass end slopes and higher characteristic masses than ours.

We can also compare our SMDs with results from studies of SFR. The evolution of star formation rate density (SFRD) also measures how galaxies grow throughout cosmic time and it is related to the evolution of stellar mass through an integration in time. However, the way studies measure SFRD is fairly independent from SMDs results and a comparison between the two can help us check the consistency in our results.

Stellar mass is an integral of past star formation, since it represents the accumulation of mass produced overtime. From Madau and Dickinson (2014) we have:

$$\frac{\mathrm{d}\rho_*}{\mathrm{d}t} = (1 - R)\psi$$

Were ψ is SFR and R is the *return fraction*, the mass fraction that is put back into the interstellar medium (ISM) and intergalactic medium (IGM) for each single stellar population. This equation can be integrated to obtain a form for the SMD derived from all the stellar masses generated in past episodes of star formation and the stellar remnants produced from evolution,

$$\rho_*(z) = (1 - R) \int_0^{t(z)} \psi \mathrm{d}t = (1 - R) \int_z^{\infty} \psi \frac{\mathrm{d}z'}{H(z')(1 + z')}$$

where $H(z') = H_0[\Omega_M(1 + z')^3 + \Omega_\Lambda]^{1/2}$, correspond to the Hubble parameter for a flat cosmology.

We use the parameterization of SFRD $\psi(z)$ from Madau and Dickinson (2014) to compute the time integral shown in Figure 3.10 as a dashed black line. The return factor $R = 0.41$, is the appropiate value for a Chabrier (2003) IMF.

Our results are in good agreement with this trend from $z \sim 5$ to $z \sim 4$, but starting at $z \sim 3$ discrepancies appear, reaching differences of ~ 0.5 dex between our results and those derived from SFRD estimates. This is a particularly interesting redshift range since this is where SFR is at its highest, showing a peak in the evolution of SFRD (Madau and Dickinson, 2014; Bouwens et al., 2015).

These discrepancies in our results and those from SFRD studies can be due to many factors. On our side, our GSMF lack a high mass galaxy contribution that could be affecting our integrated mass. To check if this effect is enough to bridge this gap in SMD we combine our GSMFs with the massive end of the GSMFs by Davidzon et al. (2017). We do this by integrating their GSMF at $1.5 < z < 2.0$ in the range $10 < \log_{10}(M_*/M_\odot) < 13$, this generated a contribution of $\log_{10}(\rho_*/M_\odot \mathrm{Mpc}^{-3}) \sim 7.4$. When we combine this mass contribution with our integrated mass at $8 < \log_{10}(M_*/M_\odot) < 10$, we are still below Madau and Dickinson (2014) by 0.2 dex, shown by the red star in Figure 3.10. So, even if we take into account the high mass galaxy population, this correction is probably not enough to explain the offset.

On the other hand as we showed in Section 2.1.1, SFR is an unreliable estimate, and the results depend strongly on the methodology and wavelength range used. Just from SED fitting the results can vary up to $\times 10^{15}$ in the most extreme cases when changing between Bayesian and MLE estimators. The change in wavelength range used in the estimations can also lead to differences produced by the different populations probed with each technique. Taking this into account, studies like Madau and Dickinson (2014) that compile results from different works could be suffering from the use of different estimators across redshifts. Thus the importance of understanding the biases the different methodologies introduce in our results and performing studies that probe this range in an homogeneous and consistent way.

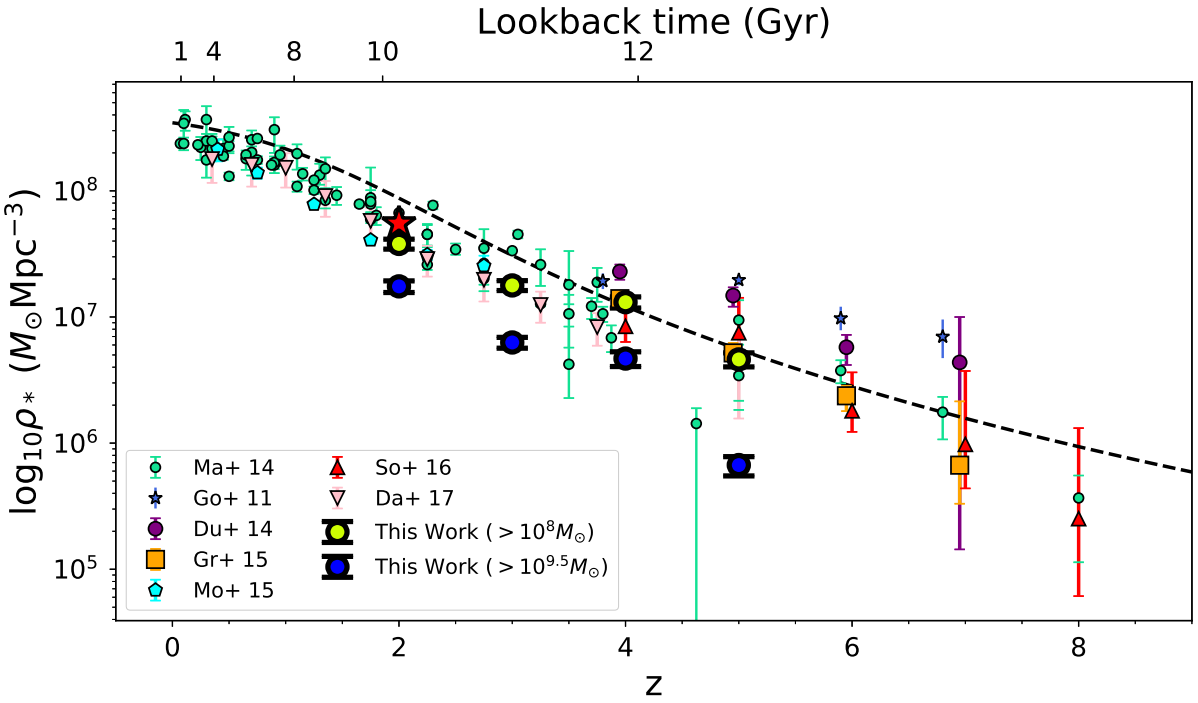

Figure 3.10: Evolution of the stellar mass density with redshift. Our stellar mass density estimations were computed by integrating the best-fit Schechter functions for our GSMFs between $M_* = 10^8 M_\odot$ and $M_* = 10^{13} M_\odot$. Yellow filled circles correspond to our estimations using single Schechter functions while in blue are the result from using a double Schechter function at the lower redshift ranges. Uncertainties were obtained by performing 10^4 repetitions perturbing our GSMFs using the posterior distributions for the Schechter parameters. Overplotted are some results from the literature. A dashed black curve indicates the predicted SMD from Madau and Dickinson (2014) SFRD using a recycling factor of $R = 0.41$.

Conclusion

In this work, we presented a study of the galaxy stellar mass functions from $z \sim 2$ to $z \sim 5$ using a sample of LBGs galaxies (Bouwens et al. 2019, in prep), that uses a wealth of published data from the HUDF/XDF, HUDF09-1, HUDF09-2 and all five CANDELS fields, obtaining a total search area of ~ 750 arcmin^2 including observations reaching as deep as 30 mag (5σ). The sample includes $\sim 20,000$ sources in the range $2 < z < 5$, which are used to compute the UV-LFs at these redshifts.

We took advantage of the robustness of these measurements to construct GSMFs that have already been treated for incompleteness and selection effects. The use of five different searching fields with independent sight lines also makes these results robust to the effects of cosmic variance.

The mid-IR data we used to estimate the stellar masses in this study correspond to the deepest Spitzer/IRAC observations available from the GREATS program (Stefanon et al. 2019, in prep), allowing us to obtain very good estimates at low-masses and constrain the low-mass end of the GSMF. We took special care to assess the impact the extra flux from nebular emission causes on our estimations of stellar mass at the highest redshifts ($z \sim 4$ and 5) and control for them. We also study the robustness of our results to the choice of estimator, comparing the stellar masses obtained from MLE and a bayesian-like method.

A summary of our main results and conclusions is as follows:

1. We find that the contribution of extra flux from rest-frame optical emission lines, mainly Hα 6562.8 Å, to the flux in our sources at $3.8 < z < 5.0$ produces an average offset in our estimated stellar masses of ~ 0.08 dex when performing SED modeling without a prescription for nebular emission.
2. We observe tight correlations between stellar mass and rest-frame UV magnitude at all redshifts in this study, and obtain a parametrisation for the trend between $\log_{10} M_*$ vs. $M_{\rm UV}$. The slopes we recover don't show an evolution with redshift but the normalization evolves with time, producing galaxies with higher mass-to-light ratios at a fixed magnitude with cosmic time.
3. From our study of the intrinsic scatter of the $\log_{10}(M_*)$–M_{UV} relation we find no strong support for a varying scatter at high redshifts. However, at the lowest redshift studied $z \sim 2$, our model comparison analysis supported a model with larger scatter at higher masses.
4. Our resulting GSMFs span a range of stellar masses from $M = 10^7 M_\odot$ to $M = 10^{11.5} M_\odot$,

that provides very good constraints for the low-mass end slope computation. We see an evolution of the shape of our GSMFs in the $2 < z < 5$ range with our GSMFs becoming steeper with redshift.

5. Results from our fitting procedure of the Schechter parameters support an evolution of the low-mass end slope α, that steepens from $\alpha = -1.54$ at $z = 2$ to $\alpha = -1.89$ at $z = 5$. This evolution is slower than what previous studies find for the same redshift range. We also find an evolution in the normalization but no evidence of the same evolution for the characteristic mass.
6. Our estimations of SMD, derived over the $8 < \log_{10}(M/M_{\odot}) < 13$ mass range, show an increase with time of ~ 1.0 dex from $z \sim 5$ to $z \sim 2$. At our highest redshifts $z \sim 4$ and 5 we find excellent agreement with the predictions from the time integral of SFRD recovered by Madau and Dickinson (2014). However, our estimates fall short at $z \sim 2$ and 3 by ~ 0.5 dex.

Daniela thanks the LSSTC Data Science Fellowship Program, which is funded by LSSTC, NSF Cybertraining Grant #1829740, the Brinson Foundation, and the Moore Foundation; her participation in the program has benefited this work. This work is based on observations taken by the 3D-HST Treasury Program (GO 12177 and 12328) with the NASA/ESA HST, which is operated by the Association of Universities for Research in Astronomy, Inc., under NASA contract NAS5-26555. This work was supported by CONICYT/FONDECYT Iniciation grant number 11160832.

Bibliography

Amorín, R., Fontana, A., Pérez-Montero, E., Castellano, M., Guaita, L., Grazian, A., Fèvre, O. L., Ribeiro, B., Schaerer, D., Tasca, L. A., Thomas, R., Bardelli, S., Cassarà, L., Cassata, P., Cimatti, A., Contini, T., Barros, S. D., Garilli, B., Giavalisco, M., Hathi, N., Koekemoer, A., Le Brun, V., Lemaux, B. C., MacCagni, D., Pentericci, L., Pforr, J., Talia, M., Tresse, L., Vanzella, E., Vergani, D., Zamorani, G., Zucca, E., and Merlin, E. (2017). Analogues of primeval galaxies two billion years after the Big Bang. *Nature Astronomy*, 1.

Ashby, M. L., Willner, S. P., Fazio, G. G., Dunlop, J. S., Egami, E., Faber, S. M., Ferguson, H. C., Grogin, N. A., Hora, J. L., Huang, J. S., Koekemoer, A. M., Labbé, I., and Wang, Z. (2015). S-Candels: The spitzer-cosmic assembly near-infrared deep extragalactic survey. survey design, photometry, and deep irac source counts. *Astrophysical Journal, Supplement Series*, 218(2):33.

Ashby, M. L., Willner, S. P., Fazio, G. G., Huang, J. S., Arendt, R., Barmby, P., Barro, G., Bell, E. F., Bouwens, R., Cattaneo, A., Croton, D., Davé, R., Dunlop, J. S., Egami, E., Faber, S., Finlator, K., Grogin, N. A., Guhathakurta, P., Hernquist, L., Hora, J. L., Illingworth, G., Kashlinsky, A., Koekemoer, A. M., Koo, D. C., Labbé, I., Li, Y., Lin, L., Moseley, H., Nandra, K., Newman, J., Noeske, K., Ouchi, M., Peth, M., Rigopoulou, D., Robertson, B., Sarajedini, V., Simard, L., Smith, H. A., Wang, Z., Wechsler, R., Weiner, B., Wilson, G., Wuyts, S., Yamada, T., and Yan, H. (2013). Seds: The spitzer extended deep survey. Survey design, photometry, and deep irac source counts. *Astrophysical Journal*, 769(1).

Barro, G., Pérez-González, P. G., Cava, A., Brammer, G., Pandya, V., Moral, C. E., Esquej, P., Domínguez-Sánchez, H., Pampliega, B. A., Guo, Y., Koekemoer, A. M., Trump, J. R., Ashby, M. L. N., Cardiel, N., Castellano, M., Conselice, C. J., Dickinson, M. E., Dolch, T., Donley, J. L., Briones, N. E., Faber, S. M., Fazio, G. G., Ferguson, H., Finkelstein, S., Fontana, A., Galametz, A., Gardner, J. P., Gawiser, E., Giavalisco, M., Grazian, A., Grogin, N. A., Hathi, N. P., Hemmati, S., Hernán-Caballero, A., Kocevski, D., Koo, D. C., Kodra, D., Lee, K.-S., Lin, L., Lucas, R. A., Mobasher, B., McGrath, E. J., Nandra, K., Nayyeri, H., Newman, J. A., Pforr, J., Peth, M., Rafelski, M., Rodríguez-Munoz, L., Salvato, M., Stefanon, M., Wel, A. v. d., Willner, S. P., Wiklind, T., and Wuyts, S. (2019). The CANDELS/SHARDS Multiwavelength Catalog in GOODS-N: Photometry, Photometric Redshifts, Stellar Masses, Emission-line Fluxes, and Star Formation Rates. *The Astrophysical Journal Supplement Series*, 243(2):22.

Bertinl, E. (1996). SExtractor: Software for source extraction. *Astronomy and Astrophysics Supplement Series*, 117(2):393–404.

Blakeslee, J., Anderson, K., Meurer, G., Benitez, N., and Magee, D. (2002). An Automatic Image Reduction Pipeline for the Advanced Camera for Surveys. *arXiv preprint astro-ph/0212362*, 295:257–260.

Boquien, M., Burgarella, D., Roehlly, Y., Buat, V., Ciesla, L., Corre, D., Inoue, A. K., and Salas, H. (2019). CIGALE: A python Code Investigating GALaxy Emission. *Astronomy and Astrophysics*, 622:1–33.

Bouwens, R. J., Illingworth, G. D., Oesch, P. A., Labbé, I., Trenti, M., Van Dokkum, P., Franx, M., Stiavelli, M., Carollo, C. M., Magee, D., and Gonzalez, V. (2011). Ultraviolet luminosity functions from 132 z 7 and z 8 lyman-break galaxies in the ultra-deep hudf09 and wide-area early release science wfc3/ir observations. *Astrophysical Journal*, 737(2).

Bouwens, R. J., Illingworth, G. D., Oesch, P. A., Trenti, M., Labbé, I., Bradley, L., Carollo, M., Van Dokkum, P. G., Gonzalez, V., Holwerda, B., Franx, M., Spitler, L., Smit, R., and Magee, D. (2015). UV luminosity functions at redshifts z 4 to z 10: 10,000 galaxies from HST legacy fields. *Astrophysical Journal*, 803(1):1–49.

Brammer, G. B., van Dokkum, P. G., and Coppi, P. (2008). EAZY: A Fast, Public Photometric Redshift Code. *The Astrophysical Journal*, 686(2):1503–1513.

Bruzual, G. and Charlot, S. (2003). Stellar population synthesis at the resolution of 2003. *Monthly Notices of the Royal Astronomical Society*, 344(4):1000–1028.

Calzetti, D. (2011). Star formation rate indicators. *Secular Evolution of Galaxies*, pages 419–458.

Caputi, K. I., Deshmukh, S., Ashby, M. L. N., Cowley, W. I., Bisigello, L., Fazio, G. G., Fynbo, J. P. U., Fevre, O. L., Milvang-Jensen, B., and Ilbert, O. (2017). Star formation in galaxies at z˜4-5 from the SMUVS survey: a clear starburst/main-sequence bimodality for Halpha emitters on the SFR-M* plane.

Chabrier, G. (2003). Galactic Stellar and Substellar Initial Mass Function. *Publications of the Astronomical Society of the Pacific*, 115(809):763–795.

Conroy, C. (2013). Modeling the Panchromatic Spectral Energy Distributions of Galaxies. *Annual Review of Astronomy and Astrophysics*, 51(1):393–455.

Davidzon, I., Ilbert, O., Laigle, C., Coupon, J., McCracken, H. J., Delvecchio, I., Masters, D., Capak, P. L., Hsieh, B. C., Tresse, L., Fevre, O. L., Bethermin, M., Chang, Y. Y., Faisst, A. L., Floc'h, E. L., Steinhardt, C., Toft, S., Aussel, H., Dubois, C., Hasinger, G., Salvato, M., Sanders, D. B., Scoville, N., and Silverman, J. D. (2017). The COSMOS2015 galaxy stellar mass function: 13 billion years of stellar mass assembly in 10 snapshots. 70.

Dickinson, M., Stern, D., Giavalisco, M., Ferguson, H. C., Tsvetanov, Z., Chornock, R., Cristiani, S., Dawson, S., Dey, A., Filippenko, A. V., Moustakas, L. A., Nonino, M., Papovich, C., Ravindranath, S., Riess, A., Rosati, P., Spinrad, H., and Vanzella, E. (2004). Color-selected Galaxies at z 6 in the Great Observatories Origins Deep Survey . *The Astrophysical Journal*, 600(2):L99–L102.

Duncan, K., Conselice, C. J., Mortlock, A., Hartley, W. G., Guo, Y., Ferguson, H. C., Davé, R., Lu, Y., Ownsworth, J., Ashby, M. L., Dekel, A., Dickinson, M., Faber, S., Giavalisco, M., Grogin, N., Kocevski, D., Koekemoer, A., Somerville, R. S., and White, C. E. (2014). The mass evolution of the first galaxies: Stellar mass functions and star formation rates at $4 < z < 7$ in the CANDELS GOODS-south field. *Monthly Notices of the Royal Astronomical Society*, 444(3):2960–2984.

Efstathiou, G., Ellis, R. S., and Peterson, B. A. (1988). Analysis of a complete galaxy redshift

survey - II. The field-galaxy luminosity function. *Monthly Notices of the Royal Astronomical Society*, 232(2):431–461.

Ellis, R. S., McLure, R. J., Dunlop, J. S., Robertson, B. E., Ono, Y., Schenker, M. A., Koekemoer, A., Bowler, R. A., Ouchi, M., Rogers, A. B., Curtis-Lake, E., Schneider, E., Charlot, S., Stark, D. P., Furlanetto, S. R., and Cirasuolo, M. (2013). The abundance of star-forming galaxies in the redshift range 8.5-12: New results from the 2012 Hubble Ultra Deep Field CAMPAIGN. *Astrophysical Journal Letters*, 763(1):8–13.

Finkelstein, S. L., Ryan, R. E., Papovich, C., Dickinson, M., Song, M., Somerville, R. S., Ferguson, H. C., Salmon, B., Giavalisco, M., Koekemoer, A. M., Ashby, M. L., Behroozi, P., Castellano, M., Dunlop, J. S., Faber, S. M., Fazio, G. G., Fontana, A., Grogin, N. A., Hathi, N., Jaacks, J., Kocevski, D. D., Livermore, R., McLure, R. J., Merlin, E., Mobasher, B., Newman, J. A., Rafelski, M., Tilvi, V., and Willner, S. P. (2015). the Evolution of the Galaxy Rest-Frame Ultraviolet Luminosity Function Over the First Two Billion Years. *Astrophysical Journal*, 810(1):71.

Fontanot, F., Lucia, G. D., Somerville, R. S., and Santini, P. (2009). The Many Manifestations of Downsizing : Hierarchical Galaxy Formation Models confront Observations . arXiv : 0901 . 1130v2 [astro-ph . CO] 13 May 2009. 000(May):1776–1790.

Foreman-Mackey, D., Hogg, D. W., Lang, D., and Goodman, J. (2013). emcee : The MCMC Hammer . *Publications of the Astronomical Society of the Pacific*, 125(925):306–312.

Giavalisco, M., Ferguson, H. C., Koekemoer, A. M., Dickinson, M., Alexander, D. M., Bauer, F. E., Bergeron, J., Biagetti, C., Brandt, W. N., Casertano, S., Cesarsky, C., Chatzichristou, E., Conselice, C., Cristiani, S., Da Costa, L., Dahlen, T., de Mello, D., Eisenhardt, P., Erben, T., Fall, S. M., Fassnacht, C., Fosbury, R., Fruchter, A., Gardner, J. P., Grogin, N., Hook, R. N., Hornschemeier, A. E., Idzi, R., Jogee, S., Kretchmer, C., Laidler, V., Lee, K. S., Livio, M., Lucas, R., Madau, P., Mobasher, B., Moustakas, L. A., Nonino, M., Padovani, P., Papovich, C., Park, Y., Ravindranath, S., Renzini, A., Richardson, M., Riess, A., Rosati, P., Schirmer, M., Schreier, E., Somerville, R. S., Spinrad, H., Stern, D., Stiavelli, M., Strolger, L., Urry, C. M., Vandame, B., Williams, R., and Wolf, C. (2004). The Great Observatories Origins Deep Survey: Initial Results from Optical and Near-Infrared Imaging. *The Astrophysical Journal*, 600(2):L93–L98.

González, V., Labbé, I., Bouwens, R. J., Illingworth, G., Franx, M., and Kriek, M. (2011). Evolution of galaxy stellar mass functions, mass densities, and mass-to-light ratios from z 7 to z 4. *Astrophysical Journal Letters*, 735(2):6–11.

Goodman, J. and Weare, J. (2010). Communications in Applied Mathematics and Computational Science ENSEMBLE SAMPLERS WITH AFFINE. *CAMCoS*, 5(1):65–79.

Grazian, A., Fontana, A., Santini, P., Dunlop, J. S., Ferguson, H. C., Castellano, M., Amorin, R., Ashby, M. L. N., Barro, G., Behroozi, P., Boutsia, K., Caputi, K. I., Chary, R. R., Dekel, A., Dickinson, M. E., Faber, S. M., Fazio, G. G., Finkelstein, S. L., Galametz, A., Giallongo, E., Giavalisco, M., Grogin, N. A., Guo, Y., Kocevski, D., Koekemoer, A. M., Koo, D. C., Lee, K.-S., Lu, Y., Merlin, E., Mobasher, B., Nonino, M., Papovich, C., Paris, D., Pentericci, L., Reddy, N., Renzini, A., Salmon, B., Salvato, M., Sommariva, V., Song, M., and Vanzella, E. (2015). The galaxy stellar mass function at 3.5 z 7.5 in the CANDELS/UDS, GOODS-South, and HUDF fields . *Astronomy & Astrophysics*, 575:A96.

Grogin, N. A., Kocevski, D. D., Faber, S. M., Ferguson, H. C., Koekemoer, A. M., Riess, A. G.,

Acquaviva, V., Alexander, D. M., Almaini, O., Ashby, M. L., Barden, M., Bell, E. F., Bournaud, F., Brown, T. M., Caputi, K. I., Casertano, S., Cassata, P., Castellano, M., Challis, P., Chary, R. R., Cheung, E., Cirasuolo, M., Conselice, C. J., Cooray, A. R., Croton, D. J., Daddi, E., Dahlen, T., Davé, R., De Mello, D. F., Dekel, A., Dickinson, M., Dolch, T., Donley, J. L., Dunlop, J. S., Dutton, A. A., Elbaz, D., Fazio, G. G., Filippenko, A. V., Finkelstein, S. L., Fontana, A., Gardner, J. P., Garnavich, P. M., Gawiser, E., Giavalisco, M., Grazian, A., Guo, Y., Hathi, N. P., Häussler, B., Hopkins, P. F., Huang, J. S., Huang, K. H., Jha, S. W., Kartaltepe, J. S., Kirshner, R. P., Koo, D. C., Lai, K., Lee, K. S., Li, W., Lotz, J. M., Lucas, R. A., Madau, P., McCarthy, P. J., McGrath, E. J., McIntosh, D. H., McLure, R. J., Mobasher, B., Moustakas, L. A., Mozena, M., Nandra, K., Newman, J. A., Niemi, S. M., Noeske, K. G., Papovich, C. J., Pentericci, L., Pope, A., Primack, J. R., Rajan, A., Ravindranath, S., Reddy, N. A., Renzini, A., Rix, H. W., Robaina, A. R., Rodney, S. A., Rosario, D. J., Rosati, P., Salimbeni, S., Scarlata, C., Siana, B., Simard, L., Smidt, J., Somerville, R. S., Spinrad, H., Straughn, A. N., Strolger, L. G., Telford, O., Teplitz, H. I., Trump, J. R., Van Der Wel, A., Villforth, C., Wechsler, R. H., Weiner, B. J., Wiklind, T., Wild, V., Wilson, G., Wuyts, S., Yan, H. J., and Yun, M. S. (2011). Candels: The Cosmic Assembly Near-infrared Deep Extragalactic Legacy Survey. *Astrophysical Journal, Supplement Series*, 197(2).

Ilbert, O., McCracken, H. J., Le Fèvre, O., Capak, P., Dunlop, J., Karim, A., Renzini, M. A., Caputi, K., Boissier, S., Arnouts, S., Aussel, H., Comparat, J., Guo, Q., Hudelot, P., Kartaltepe, J., Kneib, J. P., Krogager, J. K., Le Floc'H, E., Lilly, S., Mellier, Y., Milvang-Jensen, B., Moutard, T., Onodera, M., Richard, J., Salvato, M., Sanders, D. B., Scoville, N., Silverman, J. D., Taniguchi, Y., Tasca, L., Thomas, R., Toft, S., Tresse, L., Vergani, D., Wolk, M., and Zirm, A. (2013). Mass assembly in quiescent and star-forming galaxies since z 4 from UltraVISTA. *Astronomy and Astrophysics*, 556:55.

Illingworth, G. D., Magee, D., Oesch, P. A., Bouwens, R. J., Labbé, I., Stiavelli, M., Van Dokkum, P. G., Franx, M., Trenti, M., Carollo, C. M., and Gonzalez, V. (2013). The hst extreme deep field (XDF): Combining all acs and WFC3/IR data on the hudf region into the deepest field ever. *Astrophysical Journal, Supplement Series*, 209(1).

Kass, R. E. and Raferty, A. E. (1978). Bayesian information criterion. *Journal of the American Statistical Association*, 90(430):1–3.

Koekemoer, A. M., Faber, S. M., Ferguson, H. C., Grogin, N. A., Kocevski, D. D., Koo, D. C., Lai, K., Lotz, J. M., Lucas, R. A., McGrath, E. J., Ogaz, S., Rajan, A., Riess, A. G., Rodney, S. A., Strolger, L., Casertano, S., Castellano, M., Dahlen, T., Dickinson, M., Dolch, T., Fontana, A., Giavalisco, M., Grazian, A., Guo, Y., Hathi, N. P., Huang, K. H., Van Der Wel, A., Yan, H. J., Acquaviva, V., Alexander, D. M., Almaini, O., Ashby, M. L., Barden, M., Bell, E. F., Bournaud, F., Brown, T. M., Caputi, K. I., Cassata, P., Challis, P. J., Chary, R. R., Cheung, E., Cirasuolo, M., Conselice, C. J., Cooray, A. R., Croton, D. J., Daddi, E., Davé, R., De Mello, D. F., De Ravel, L., Dekel, A., Donley, J. L., Dunlop, J. S., Dutton, A. A., Elbaz, D., Fazio, G. G., Filippenko, A. V., Finkelstein, S. L., Frazer, C., Gardner, J. P., Garnavich, P. M., Gawiser, E., Gruetzbauch, R., Hartley, W. G., Häussler, B., Herrington, J., Hopkins, P. F., Huang, J. S., Jha, S. W., Johnson, A., Kartaltepe, J. S., Khostovan, A. A., Kirshner, R. P., Lani, C., Lee, K. S., Li, W., Madau, P., McCarthy, P. J., McIntosh, D. H., McLure, R. J., McPartland, C., Mobasher, B., Moreira, H., Mortlock, A., Moustakas, L. A., Mozena, M., Nandra, K., Newman, J. A., Nielsen, J. L., Niemi, S., Noeske, K. G., Papovich, C. J., Pentericci, L., Pope, A., Primack, J. R., Ravindranath, S., Reddy, N. A., Renzini, A., Rix, H. W., Robaina, A. R., Rosario, D. J., Rosati, P., Salimbeni, S., Scarlata, C., Siana, B., Simard, L., Smidt, J., Snyder, D., Somerville, R. S., Spinrad, H., Straughn,

A. N., Telford, O., Teplitz, H. I., Trump, J. R., Vargas, C., Villforth, C., Wagner, C. R., Wandro, P., Wechsler, R. H., Weiner, B. J., Wiklind, T., Wild, V., Wilson, G., Wuyts, S., and Yun, M. S. (2011). Candels: The cosmic assembly near-infrared deep extragalactic legacy survey - The hubble space telescope observations, imaging data products, and mosaics. *Astrophysical Journal, Supplement Series*, 197(2).

Kron, R. G. (1980). Photometry of a complete sample of faint galaxies. *The Astrophysical Journal Supplement Series*, 43(September):305.

Labbé, I., Bouwens, R., Illingworth, G. D., and Franx, M. (2006). Spitzer IRAC Confirmation of z 850 -Dropout Galaxies in the Hubble Ultra Deep Field: Stellar Masses and Ages at z 7 . *The Astrophysical Journal*, 649(2):L67–L70.

Labbé, I., González, V., Bouwens, R. J., Illingworth, G. D., Franx, M., Trenti, M., Oesch, P. A., Van Dokkum, P. G., Stiavelli, M., Carollo, C. M., Kriek, M., and Magee, D. (2010a). Star formation rates and stellar masses of z = 7-8 galaxies from IRAC observations of the WFC3/IR early release science and the HUDF fields. *Astrophysical Journal Letters*, 716(2 PART 2).

Labbé, I., Gonzalez, V., Bouwens, R. J., Illingworth, G. D., Oesch, P. A., Van Dokkum, P. G., Carollo, C. M., Franx, M., Stiavelli, M., Trenti, M., Magee, D., and Kriek, M. (2010b). Ultradeep infrared array camera observations of sub-L* z7 and z8 galaxies in the hubble ultra deep field: The contribution of low-luminosity galaxies to the stellar mass density and reionization. *Astrophysical Journal Letters*, 708(1 PART 2):26–31.

Labbé, I., Oesch, P. A., Bouwens, R. J., Illingworth, G. D., Magee, D., González, V., Carollo, C. M., Franx, M., Trenti, M., Van Dokkum, P. G., and Stiavelli, M. (2013). The spectral energy distributions of z 8 galaxies from the IRAC ultra deep fields: Emission lines, stellar masses, and specific star formation rates at 650 MYR. *Astrophysical Journal Letters*, 777(2):6–11.

Madau, P. and Dickinson, M. (2014). Cosmic Star Formation History. pages 415–488.

Magee, D. K., Bouwens, R. J., and Illingworth, G. D. (2011). WFC3RED : A HST Wide Field Camera 3 Image Processing Pipeline Creates final CR-cleaned , distortion-free drizzled image mosaics using MultiDrizzle Refines the final output image WCS (if needed). *Astronomical Data Analysis Software and Systems XX*, 442:395–398.

Marchesini, D., Van Dokkum, P. G., Förster Schreiber, N. M., Franx, M., Labbé, I., and Wuyts, S. (2009). The evolution of the stellar mass function of galaxies from z = 4.0 and the first comprehensive analysis of its uncertainties: Evidence for mass-dependent evolution. *Astrophysical Journal*, 701(2):1765–1796.

Meurer, G. R., Heckman, T. M., and Calzetti, D. (1999). Dust Absorption and the Ultraviolet Luminosity Density at z 3 as Calibrated by Local Starburst Galaxies . *The Astrophysical Journal*, 521(1):64–80.

Mortlock, A., Conselice, C. J., Hartley, W. G., Duncan, K., Lani, C., Ownsworth, J. R., Almaini, O., Van Der Wel, A., Huang, K. H., Ashby, M. L., Willner, S. P., Fontana, A., Dekel, A., Koekemoer, A. M., Ferguson, H. C., Faber, S. M., Grogin, N. A., and Kocevski, D. D. (2015). Deconstructing the galaxy stellar mass function with UKIDSS and CANDELS: The impact of colour, structure and environment. *Monthly Notices of the Royal Astronomical Society*, 447(1):2–24.

Noeske, K. G., Faber, S. M., Weiner, B. J., Koo, D. C., Primack, J. R., Dekel, A., Papovich, C., Conselice, C. J., Le Floc'h, E., Rieke, G. H., Coil, A. L., Lotz, J. M., Somerville, R. S., and Bundy, K. (2007). Star Formation in AEGIS Field Galaxies since z = 1.1: Staged Galaxy Formation and a Model of Mass-dependent Gas Exhaustion . *The Astrophysical Journal*, 660(1):L47–L50.

Noll, S., Burgarella, D., Giovannoli, E., Buat, V., Marcillac, D., and Muñoz-Mateos, J. C. (2009). Astrophysics Analysis of galaxy spectral energy distributions from far-UV to far-IR with CIGALE: studying a SINGS test sample. *a&a*, 507:1793–1813.

Oesch, P. A., Bouwens, R. J., Illingworth, G. D., Labbé, I., Franx, M., Van Dokkum, P. G., Trenti, M., Stiavelli, M., Gonzalez, V., and Magee, D. (2013). Probing the dawn of galaxies at z 9-12: New constraints from HUDF12/XDF and candels data. *Astrophysical Journal*, 773(1).

Oesch, P. A., Brammer, G., Dokkum, P. G. v., Illingworth, G. D., Bouwens, R. J., Labbé, I., Franx, M., Momcheva, I., Ashby, M. L. N., Fazio, G. G., Gonzalez, V., Holden, B., Magee, D., Skelton, R. E., Smit, R., Spitler, L. R., Trenti, M., and Willner, S. P. (2016). a Remarkably Luminous Galaxy At Z = 11.1 Measured With Hubble Space Telescope Grism Spectroscopy . *The Astrophysical Journal*, 819(2):129.

Oesch, P. A., Montes, M., Reddy, N., Bouwens, R. J., Illingworth, G. D., Magee, D., Atek, H., Carollo, C. M., Cibinel, A., Franx, M., Holden, B., Labbé, I., Nelson, E. J., Steidel, C. C., van Dokkum, P. G., Morselli, L., Naidu, R. P., and Wilkins, S. (2018). HDUV: The Hubble Deep UV Legacy Survey. *The Astrophysical Journal Supplement Series*, 237(1):12.

Papovich, C., Dickinson, M., and Ferguson, H. C. (2001). The Stellar Populations and Evolution of Lyman Break Galaxies. *The Astrophysical Journal*, 559(2):620–653.

Salmon, B., Papovich, C., Finkelstein, S. L., Tilvi, V., Finlator, K., Behroozi, P., Dahlen, T., Davé, R., Dekel, A., Dickinson, M., Ferguson, H. C., Giavalisco, M., Long, J., Lu, Y., Mobasher, B., Reddy, N., Somerville, R. S., and Wechsler, R. H. (2015). The relation between star formation rate and stellar mass for galaxies at 3.5 & le; z & le; 6.5 in candels. *Astrophysical Journal*, 799(2).

Salpeter, E. E. (1955). THE LUMINOSITY FUNCTION AND STELLAR EVOLUTION Edwin E. Salpeter* Australian National University, Canberra, and Cornell University Received July 29, 1954. *The Astrophysical Journal*, 121:161–167.

Sandage, A., Tammann, G. A., and Yahil, A. (1979). The velocity field of bright nearby galaxies. I - The variation of mean absolute magnitude with redshift for galaxies in a magnitude-limited sample. *The Astrophysical Journal*, 232(September):352.

Santini, P., Fontana, A., Grazian, A., Salimbeni, S., Fontanot, F., Paris, D., Boutsia, K., Castellano, M., Fiore, F., Gallozzi, S., Giallongo, E., Koekemoer, A. M., Menci, N., Pentericci, L., and Somerville, R. S. (2012). The evolving slope of the stellar mass function at .6 z $<$ 4.5 from deep WFC3 data. *Astronomy and Astrophysics*, 538:1–13.

Schaerer, D. and De Barros, S. (2009). The impact of nebular emission on the ages of z 6 galaxies. *Astronomy and Astrophysics*, 502(2):423–426.

Schaerer, D. and De Barros, S. (2010). On the physical properties of z 6-8 galaxies. *Astronomy and Astrophysics*, 515(8):1–15.

Schechter, P. C. I. o. T. (1976). An analytic expression for the luminosity function for galaxies. *Astrophysical Journal*, 203(1):297–306.

Schmidt, M. (1968). Space Distribution and Luminosity Functions of Quasi-Stellar Radio Sources. *The Astrophysical Journal*, 151(February):393.

Shapley, A. E., Reddy, N. A., Kriek, M., Freeman, W. R., Sanders, R. L., Siana, B., Coil, A. L., Mobasher, B., Shivaei, I., Price, S. H., and Groot, L. D. (2015). The mosdef survey: Excitation properties of z 2.3 star-forming galaxies. *Astrophysical Journal*, 801(2):88.

Skelton, R. E., Whitaker, K. E., Momcheva, I. G., Brammer, G. B., Van Dokkum, P. G., Labbé, I., Franx, M., Van Der Wel, A., Bezanson, R., Da Cunha, E., Fumagalli, M., Förster Schreiber, N., Kriek, M., Leja, J., Lundgren, B. F., Magee, D., Marchesini, D., Maseda, M. V., Nelson, E. J., Oesch, P., Pacifici, C., Patel, S. G., Price, S., Rix, H. W., Tal, T., Wake, D. A., and Wuyts, S. (2014). 3D-HST WFC3-selected photometric catalogs in the five candels/3D-HST fields: Photometry, photometric redshifts, and stellar masses. *Astrophysical Journal, Supplement Series*, 214(2).

Somerville, R. S. and Davé, R. (2015). Physical Models of Galaxy Formation in a Cosmological Framework. *Annual Review of Astronomy and Astrophysics*, 53(1):51–113.

Sommariva, V., Mannucci, F., Cresci, G., Maiolino, R., Marconi, A., Nagao, T., Baroni, A., and Grazian, A. (2012). Stellar metallicity of star-forming galaxies at z 3. *Astronomy and Astrophysics*, 539.

Song, M., Finkelstein, S. L., Ashby, M. L. N., Grazian, A., Lu, Y., Papovich, C., Salmon, B., Somerville, R. S., Dickinson, M., Duncan, K., Faber, S. M., Fazio, G. G., Ferguson, H. C., Fontana, A., Guo, Y., Hathi, N., Lee, S.-K., Merlin, E., and Willner, S. P. (2016). THE EVOLUTION OF THE GALAXY STELLAR MASS FUNCTION AT z = 4–8: A STEEPENING LOW-MASS-END SLOPE WITH INCREASING REDSHIFT . *The Astrophysical Journal*, 825(1):5.

Speagle, J. S. (2019). dynesty: A Dynamic Nested Sampling Package for Estimating Bayesian Posteriors and Evidences. 28(April):1–28.

Stark, D. P., Ellis, R. S., Charlot, S., Chevallard, J., Tang, M., Belli, S., Zitrin, A., Mainali, R., Gutkin, J., Vidal-García, A., Bouwens, R., and Oesch, P. (2017). Lyα and CIII] emission in z = 7-9 Galaxies: Accelerated reionization around luminous star-forming systems? *Monthly Notices of the Royal Astronomical Society*, 464(1):469–479.

Stark, D. P., Schenker, M. A., Ellis, R., Robertson, B., McLure, R., and Dunlop, J. (2013). Keck spectroscopy of 3 < z < 7 faint lyman break galaxies: The importance of nebular emission in understanding the specific star formation rate and stellar mass density. *Astrophysical Journal*, 763(2).

Teplitz, H. I., Rafelski, M., Kurczynski, P., Bond, N. A., Grogin, N., Koekemoer, A. M., Atek, H., Brown, T. M., Coe, D., Colbert, J. W., Ferguson, H. C., Finkelstein, S. L., Gardner, J. P., Gawiser, E., Giavalisco, M., Gronwall, C., Hanish, D. J., Lee, K. S., De Mello, D. F., Ravindranath, S., Ryan, R. E., Siana, B. D., Scarlata, C., Soto, E., Voyer, E. N., and Wolfe, A. M. (2013). UVUDF: Ultraviolet imaging of the Hubble Ultra Deep Field with wide-field camera 3. *Astronomical Journal*, 146(6).

Vogelsberger, M., Genel, S., Sijacki, D., Torrey, P., Springel, V., and Hernquist, L. (2013). A model for cosmological simulations of galaxy formation physics. *Monthly Notices of the Royal Astronomical Society*, 436(4):3031–3067.

Weinmann, S. M., Pasquali, A., Oppenheimer, B. D., Finlator, K., Mendel, J. T., Crain, R. A., and MacCiò, A. V. (2012). A fundamental problem in our understanding of low-mass galaxy evolution. *Monthly Notices of the Royal Astronomical Society*, 426(4):2797–2812.

Whitaker, K. E., Franx, M., Leja, J., Van Dokkum, P. G., Henry, A., Skelton, R. E., Fumagalli, M., Momcheva, I. G., Brammer, G. B., Labbé, I., Nelson, E. J., and Rigby, J. R. (2014). Constraining the low-mass slope of the star formation sequence at $0.5 < z < 2.5$. *Astrophysical Journal*, 795(2).

Zitrin, A., Labbé, I., Belli, S., Bouwens, R., Ellis, R. S., Roberts-Borsani, G., Stark, D. P., Oesch, P. A., and Smit, R. (2015). Lyα emission from a luminous $z = 8.68$ galaxy: Implications for galaxies as tracers of cosmic reionization. *Astrophysical Journal Letters*, 810(1):L12.